Towards the virtual twin of epileptic patients with DBS:

Modelling personalised epileptiform dynamics in The Virtual Brain framework using simulation-based inference

University of Twente

Faculty of Science & Technology, Biomedical Engineering

Clinical Neurophysiology Group

Master Thesis

Elike Morsink

s2345048

Supervisors:

Dr. rer. nat. M.C. Piastra
Prof. dr. ir. M.J.A.M. van Putten
Dr. ir. B.C. Schwab
Dr. M.C. Tjepkema-Cloostermans
N.V. Chaplinskaia, MSc

Date: February 12, 2025

Abstract

Introduction: Epilepsy is a chronic neurological disorder characterised by recurrent seizures. Approximately 30% of the patients are resistant to drug therapy, the primary choice of treatment. Neurostimulation techniques such as deep brain stimulation (DBS) represent alternative treatment options, but it is not efficacious in 30% of the patients. DBS parameters are based on trial and error, and the underlying mechanisms are still far from understood. To address these issues, we draw on computational models where, ideally, both DBS effects and epileptic events can be simulated and studied. This study explored how a personalised whole-brain model generating epileptiform activity in The Virtual Brain (TVB) platform can be constructed while enabling electrophysiological data for subsequent data-fitting methods.

Methods: A build-up of the TVB involves a network-based approach, where structural connectivity from neuroimaging data and mesoscopic models are used to generate synthetic macroscopic signals comparable to empirical data. The TVB demonstration dataset was assigned for the structural connectivity in the developed model. The Epileptor model was used to simulate the cluster of nodes. One node was assigned with the ability to generate interictal epileptiform discharges (IEDs). Altogether, this formed the TVB-Epileptor model. With simulation-based inference (SBI), we applied a data-fitting method based on neural network training to detect parameter configurations that allowed patient-specific simulations.

Results: Three separate SBI analyses were conducted by training three neural networks. We assigned parameter variation to the node generating epileptiform activity, with three out of ten parameters related to epileptiform characteristics. The first analysis concerned synthetic data fitting only, showing that the SBI can converge towards a reference parameter configuration and that this results in visually similar simulations. We used the same neural network to infer the parameters for real measured data of one subject, aiming to simulate a short 5-second simulation closer to the healthy and IED-observed EEG patterns, e.g. change in signal amplitude from normal to IED-like behaviour. With the results, we found the SBI-estimated parameter configurations did not meet this aim in any way, showing neither the IED duration nor the amplitude transition overlapped. The third analysis introduced the transformation from the high-dimensional fitting of time series towards 3-dimensional feature fitting, capturing the IED duration, IED count, and the cumulative duration of the healthy intervals. We trained a 5-second and 15-second simulation-based neural network. These features were replicated successfully by SBI-estimated configurations, where we improved robustness by analysing a second subject. However, limitations were observed, as IED durations must fall within a specific range relative to the total simulated duration for both neural networks.

Conclusion: These findings highlight the ability to combine TVB and SBI to examine parameter optimisation using SBI based on real epileptiform data. The results underscore the need for methodological refinements of the TVB-Epileptor to capture broader empirical EEG characteristics. Future work should aim to integrate patient-specific connectivity and expand the explored parameter range for data-fitting purposes. In addition, exploring the integration of different or complementary modelling frameworks should be involved to improve the biological realism, flexibility, and accuracy of the personalised TVB-Epileptor model.

Contents

1 Introduction

Epilepsy is a chronic neurological disorder characterised by an increased likelihood of recurrent, unprovoked seizures, typically caused by abnormal excessive and synchronised activity in the brain [1]. Causes include genetic factors, brain injuries, infections, and structural abnormalities. Symptoms vary greatly depending on the neural circuits involved and may include convulsions, sensory disturbances, unusual behaviour, or loss of consciousness, all of which can impact the quality of life. With about 1% of the population suffering from epilepsy, it is one of the most common neurological disorders [2]. This highlights its considerable impact and the critical need for effective treatments.

The first line of treatment, antiepileptic drugs (AEDs), effectively controls seizures for the majority of the population. However, 20%-30% of the patients suffer from drug-resistant epilepsy [3]. In this population, sufficient effect in seizure reduction is not observed, resulting in the demand for alternative treatment options. One alternative is resective surgery. However, depending on the type of epilepsy, this is not always a possibility (e.g. when vital regions for essential functioning are involved). In such cases, further innovative approaches are considered, including neuromodulation.

Neuromodulation refers to utilizing implantable and non-implantable technologies, electrical or chemical, to improve the quality of life and functioning of humans [4]. The field encompasses a range of invasive and non-invasive neurostimulation techniques designed to activate the nervous system. Deep brain stimulation (DBS) is one particular invasive neurostimulation technique. The methodology is based on delivering electrical stimulation to specific brain targets to reduce seizure frequency. One DBS trial targeting the anterior nucleus of the thalamus (ANT) showed a gradual improvement with a median seizure reduction of 69% and seizure reduction for the most severe seizure type of 75%, both analysed at 5 years [5]. Another trial targeted the ANT and hippocampus (HC) regions, achieving at least a 50% reduction in seizure frequency [6].

Despite the demonstrated successes in patients, challenges remain. The mechanisms underlying the efficacy of DBS remain poorly understood. This knowledge gap contributes to the variability in treatment response, with approximately 30% of patients experiencing no adequate reduction in seizure occurrences [5]. Furthermore, parameter selection, e.g. frequency, voltage, current and pulse width, relies heavily on trial-and-error-based methods [6]. This time-consuming process delays possible benefits due to treatment while leaving patients with suboptimal outcomes.

Advancements in computational modelling have the potential to address these challenges by developing in silico whole-brain models. Platforms such as The Virtual Brain (TVB) allow integration of patient-specific structural and functional data, e.g. magnetic resonance imaging (MRI) and electroencephalogram (EEG), respectively. This enables simulations of personalised whole-brain dynamics. By modelling interconnected brain regions (nodes) and their dynamics, TVB allows the exploration of brain activity under various conditions, including DBS [7].

Multiple models have been developed to capture temporal and spatial dynamics of neural activity, specifically related to epilepsy, by describing the pathological behaviour as transitions from normal to abnormal states [8]. The Virtual Epileptic Patient (VEP) framework proposed by Jirsa *et al.* aligns with this [9]. Phenomenological models are utilized, focusing on observed dynamics of seizure initiation and propagation rather than the direct description of the underlying biological mechanisms. By simulating the progression and propagation of seizures, VEP enabled personalised predictions of seizure patterns, where understanding epilepsy as a disorder of dynamic transitions plays an important role. This conceptual framework opens the door to extending such strategies. Possibly, this includes simulations of DBS to enhance our understanding of its mechanisms and optimize therapeutic interventions.

1.1 Overall project and goal

This thesis is part of a broader project corresponding to the challenges found in epileptic patients with DBS. In this overall project, the development of a personalised DBS-treated epileptic patient model using empirical data is explored. Combining personalised whole-brain modelling (based on MRI and scalp or intracranial EEG data) with virtual DBS, we aim to improve our understanding of seizure generation, propagation, and termination under various DBS parameter scenarios. Furthermore, it can lead to a better understanding of what mechanisms underlie the distinction between effective and ineffective DBS treatment.

Performing this takes place in the TVB platform, dividing the modelling process into two steps as outlined in Figure 1. The data comes from the EANSkE study, allowing access to structural data from MRI recordings for constructing the personalised network model. Furthermore, functional data with electrocardiography recordings, 64-channel scalp EEG or intracranial EEG (iEEG) are available. When stimulation with the iEEG electrodes is activated, the scalp EEG recordings are used to develop a DBS-implanted model using a non-epileptic (healthy) network. Turning the stimulation off, simultaneous scalp EEG and iEEG recordings of epileptiform activity are available to create an epileptiform-generating model. The final step is to combine these models. This results in a personalised data-driven model that can mimic epileptiform activity per patient where DBS can be applied in the ANT region, aiming towards a better understanding of the seizure likelihood influenced by different DBS parameter settings.

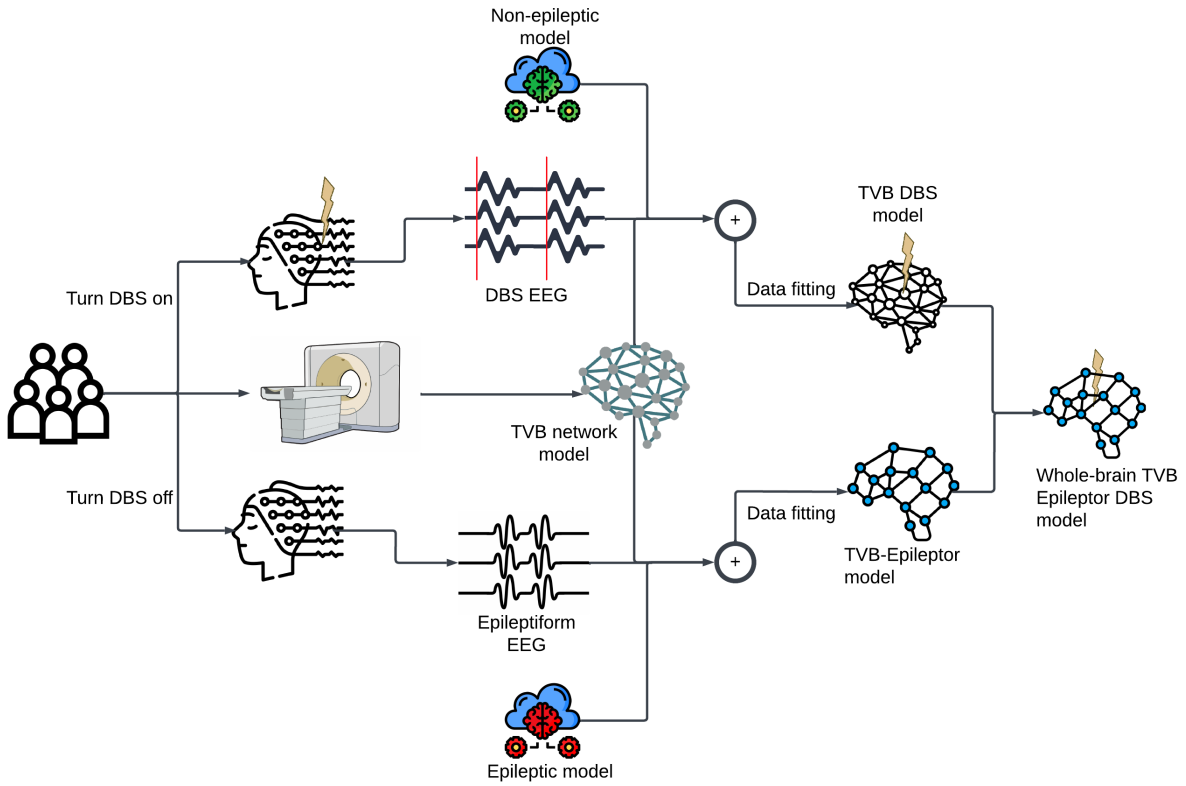

Figure 1: Overview of the overall project design towards developing a whole-brain computational model generating epileptiform activity, with virtual applied DBS implementation. Structural and functional MRI data can be used to construct a network model with personalised connectivity patterns. Then, the process is split up into two steps where the merged whole-brain TVB-Epileptor DBS model is created from i) a healthy DBS model and ii) the epileptiform generating TVB-Epileptor model.

1.2 Thesis objectives

Particularly in this thesis, we want to explore how a personalised epileptiform whole-brain model in TVB can be created, temporarily excluding the implementation of DBS. Using the Epileptor neural mass model, we aim to simulate both healthy and epileptiform activity across different brain regions, forming what is referred to as the TVB-Epileptor model. Subsequently, we will use the EANSkE data for machine learning methods to optimize model parameters. The primary research question guiding this thesis is:

How can a personalised whole-brain epileptiform model be developed and optimised to simulate (features of) epileptiform activity using the TVB platform?

To address this, the research question is divided into two sub-questions:
a) What steps are required to develop a whole-brain personalised computational macro-scale model for simulating epileptiform activity?
b) In what way can we integrate empirical iEEG data towards parameter optimisation of the TVB-Epileptor model?

Chapters 2 (Theoretical Background), 3 (Methods) and 4 (Results) of this report are structured around these sub-questions. The first part of these chapters addresses sub-question (a), focusing on developing the computational model. The second part explores sub-question (b), explaining and discussing the data-fitting methodology used to optimize the model.

2 Theoretical Background

2.1 Epilepsy

2.1.1 Definition, treatment and diagnosis

Epilepsy is a chronic neurological disorder characterised by the increased likelihood of unprovoked recurrent seizures [10]. This is the result of abnormal activity in the brain, which typically involves neuronal hyperexcitability and hypersynchrony within neural networks. These mechanisms lead to sudden bursts of electrical discharges, where in the case of unprovoked seizures, known triggers are absent (e.g. an underlying disease, low blood sugar levels, or a recent stroke). A seizure is hypothesized to occur when the brain's balance between excitation and inhibition is disrupted, which lowers the threshold for abnormal activity and, therefore, leads to hyperexcitability [11]. Seizures vary widely in both type and severity, ranging from brief lapses in awareness or jerky movements to full-body convulsions. The International League Against Epilepsy (ILAE) classifies signs of clinical manifestation by the anatomical origin of the seizures. This origin varies from i) focal (regarding one specific area), ii) generalised (with a propagation pattern affecting both brain hemispheres), or iii) of unknown cause. With a prevalence of 1%, epilepsy is known as one of the most common neurological disorders [12], [13].

Approximately 70% of the population can be treated effectively with anti-seizure medications. The remaining 30% of epilepsy patients suffer from drug-resistant epilepsy (DRE) or refractory seizures, which is hypothesised to be caused by different cellular mechanisms. The ILAE has defined drug-resistant epilepsy as a failure of adequate trials of anti-epileptic drugs of which at least two are properly chosen, used, and tolerated. According to Kwan *et al.*, the involved cellular mechanisms can broadly be characterised into several groups [13]. This includes e.g. failure of drugs to reach their targets due to overexpression of specialised proteins (efflux transporters) at the blood-brain barrier. Further proposed mechanisms include alteration in the cellular drug targets decreasing their sensitivity, and missing the appropriate target related to the pathogenic process of the patient. Refractory seizures carry a great burden of disability and a poor quality of life, as well as increased morbidity and mortality for the patient. Resective surgery is the first-line treatment for patients with DRE, though it may be contraindicated or ineffective in some cases. DBS has therefore emerged as an important alternative option [6].

2.1.2 Deep Brain Stimulation (DBS)

DBS delivers electrical stimulation to subcortical brain structures via implanted electrodes connected to a pulse generator. The electrical current can be applied in monopolar mode (i.e. between one electrode and the pulse generator), bipolar mode (between two electrodes) or multipolar configurations (involving several electrodes). The stimulation shape is defined by parameters such as frequency, amplitude and pulse width with, additional factors including unilateral versus bilateral stimulation and cycling versus continuous stimulation. An increasingly wide range of neurologic and psychiatric disorders can be treated using DBS, including Parkinson's disease, dystonia, obsessive-compulsive disorder and epilepsy [14].

Clinical trials in epilepsy also have demonstrated the efficacy of DBS. One DBS trial targeting the anterior nucleus of the thalamus (ANT) showed a gradual improvement with a median percent seizure reduction of 69% and seizure reduction for the most severe seizure type of 75%, both analysed at 5 years [5]. Another trial targeted the ANT and hippocampus (HC) regions, achieving at least a 50% reduction in seizure frequency [6]. However, a complete understanding of the therapeutic mechanisms remains unknown, and biomarkers to predict response to neuromodulation therapies are lacking. Also, high-level evidence to aid decision-making in stimulation settings is lacking, leading to time-consuming trial-and-error-based methods for optimisation procedures. These knowledge gaps contribute to withhold DRE patients from optimal seizure reduction or treatment response at all.

2.1.3 Role of EEG and Interictal Epileptiform Discharges (IEDs)

An EEG plays a central role in the diagnosis and management of patients with seizure disorders. It is a convenient and inexpensive way to demonstrate the abnormal cortical excitability associated with epilepsy [15]. It helps determine seizure type and epilepsy syndrome in patients and is thereby the proper choice of anti-seizure medication and prediction of prognosis. Furthermore, it can contribute to further classification of the diagnosis, e.g. the specific type of epilepsy syndrome or whether the seizure disorder is focal or generalised.

Particularly in this project, interictal epileptiform discharges (IEDs) are considered, known as transient electrophysiological events frequently observed in EEG recordings of epilepsy patients. IEDs occur far more often than seizures, characterised by sharp or spiky waveforms distinct from the surrounding background activity [16]. The exact relation to seizure characteristics such as frequency and spatiotemporal patterns is still debatable. Nevertheless, studies suggest that IEDs share spatial and temporal features with seizures, particularly in cortical regions involved in seizure onset [17], [18]. For instance, dense clusters of IEDs may overlap with seizure-initiation zones, and variations in IED frequency often correlate with seizure likelihood. Moreover, a recent study showed fundamental spatiotemporal similarity between IEDs and ictal discharges where was implied that most IEDs arise in brain tissue outside the site of seizure onset and propagate toward it [16].

The International Federation of Clinical Neurophysiology (IFCN) has proposed criteria to standardize IED identification [19]. This includes di- or tri-phasic wave morphology, disruption of background activity, asymmetrical waveforms, and the presence of a transient followed by a slow after-wave. These criteria have recently been validated for high diagnostic accuracy. The dataset available from the EANSkE study will provide IED recordings that will be processed and used further in the model development.

2.1.4 The EANSkE study

The main goal of the EANSkE study is to derive biomarkers from iEEG recordings via DBS electrodes to understand their association with treatment response. The study hypothesises that network analyses of structural (i.e. resting-state fMRI) and functional (i.e. scalp and intracranial EEG) brain data can provide insights into the disrupted brain dynamics in epileptic patients with DBS.

As a general classification, implanted electrodes can be composed of electrode arrays placed on the brain's surface, which we call electrocorticography (ECoG). Alternatively, shafts are utilised that penetrate deep brain structures for i) recordings, which is referred to as stereotactic EEG (sEEG) or ii) DBS, which is referred to as DBS/iEEG electrodes for stimulation and recording purposes, respectively [20]. In the EANSkE study, two shafts of 4-channel electrodes are implanted in the ANT to facilitate both recordings (iEEG) and neurostimulation (DBS) purposes.

The available data is collected from 20 patients treated at the Medisch Spectrum Twente hospital (Figure 2). The protocol included multi-modal data collection across three distinct time points: i) baseline (before DBS implantation), ii) one or two days postoperative and iii) at 12 or 24 months postoperative. Data acquisition involved simultaneous 64-channel scalp EEG, 8-channel iEEG and ECG recordings. Anatomical, fMRI and diffusion tensor imaging (DTI) scans were taken at baseline and 12 or 24 months postoperatively. Patients were asked to fill in four questionnaires related to psychological well-being at baseline and at 12 and 24 months postoperatively.

In this thesis, we will utilize the iEEG recordings to identify and characterize IED patterns. Using computational modelling techniques, we aim to replicate these patterns in silico, which involve transient disruptions of normal background activity. This contributes to the broader aim of better understanding the dynamics underlying epilepsy.

2.2 Computational modelling

Computational models provide a unique framework in which experimental data can be integrated to develop new hypotheses, which in turn can guide future experiments [21]. They can be used to identify relationships between key variables in a set of differential equations and offer a method of linking brain networks towards whole-brain models. This can particularly be valuable for epilepsy in identifying mechanisms that influence the initiation, propagation and termination patterns of epileptic seizures. Typically, computational epilepsy models operate on different scaling levels, capturing different mechanisms involved in exposure of epileptic seizures. This section introduces the terminology used in multi-scale modelling and highlights why dynamical systems are suited, especially for epilepsy.

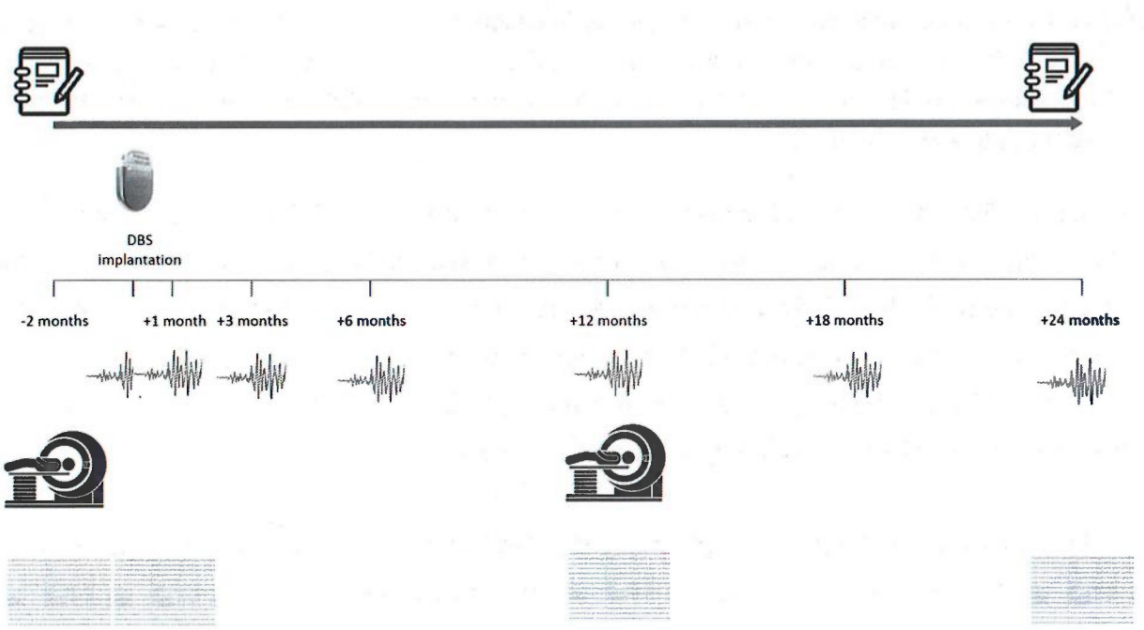

Figure 2: Overview of the study protocol used in the EANSkE study. Two months prior and one or two years after DBS implantation, MRI scans were acquired. EEG recordings were conducted at these same time points, with additional recordings one or two days postoperatively.

2.2.1 Multi-scale modelling

In Sporns *et al.*, three key levels are defined to describe different scales of brain modelling in spatial space, an overview of which is found in Figure 3 [22]. First, there is the micro-scale level, where individual synaptic connections link individual neurons. Experimentally, single-cell phenomena are analysed that can reveal, e.g. intracellular membrane potential and ion concentration changes. Also, when used in modelling (e.g. single neuron models), it can be critical for understanding the cellular and molecular mechanisms [23]. Secondly, networks connecting neuronal populations involve the mesoscale. At this level, recordings from multiple neurons or neuronal fields provide essential information about the activity distribution inside local microcircuits. It is useful for exploring how groups of neurons behave on average and interact within a specific brain region, described e.g. by a neural mass model [24]. Thirdly, when we link brain regions based on reconstructed trajectories, large-scale networks are created that operate at the macro-scale. These brain regions consist of very large numbers of neurons and neuronal populations. They are functional modelled areas, referred to as nodes, and are interconnected by fiber pathways, which form large-scale patterns of anatomical connectivity. Recording techniques at macro-scale allow in-vivo data acquisition typically used in human studies, including EEG, MRI, and positron emission tomography (PET). Altogether, it can model whole-brain activity. An example involves the so-called forward problem in EEG source analysis. This technique uses a volume conductor model (representing the head's geometry) and a source model (creating a list of source positions in the grey matter) [25], [26]. Electrodes are localized at the scalp surface and form the electrode position. Altogether, this forms the forward model, where the scalp potential at an electrode positioned on the scalp is measured due to a dipole with a dipole moment and position [27].

This project aims to implement a multi-scale model for whole-brain simulations in the TVB. In this approach, mesoscale neural mass models (Epileptor) define the functional node dynamics, while structural connectivity patterns define the large-scale network architecture of the macro-scale model. Integrating these mesoscale models into a whole-brain network allows the study of multi-scale brain dynamics.

Future work could expand this model towards an extended multi-scale framework where we incorporate micro-scale neuronal dynamics (e.g., single-neuron or synapse-level models) within key nodes, which can generate epileptiform activity. This would allow for a representation of brain activity that is spatially extended, where we integrate processes from multiple levels (ranging from fine-grained cellular mechanisms to macro-scale network interactions).

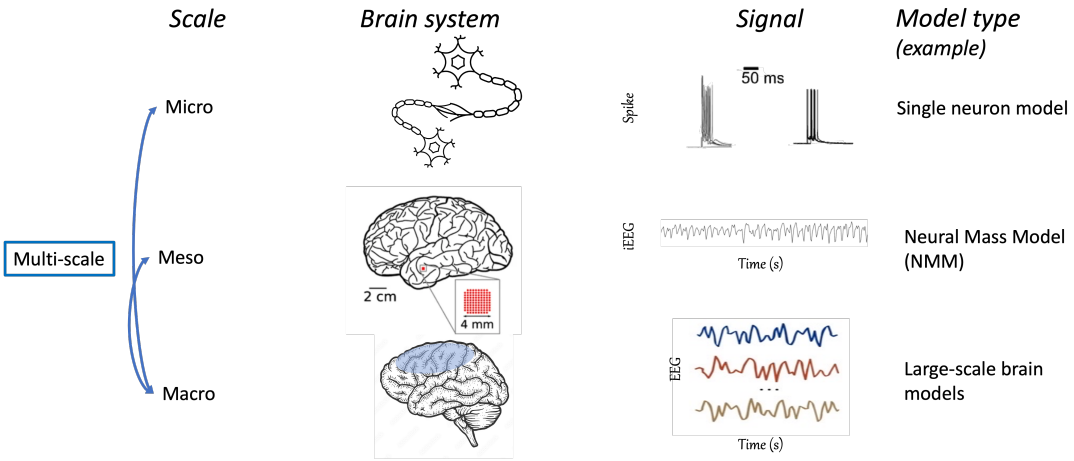

Figure 3: Overview of the different spatial scales (micro, meso and macro) used in computational modelling, where the multi-scale is defined as a combination of two different spatial scales. A schematic visualisation of the corresponding biological representation of the brain system is illustrated schematically. The signals represent examples of (in vitro or in vivo) experimentally measured neuronal activities, and the model column provides examples of in silico model types corresponding to each scale.

2.2.2 The Virtual Brain

The Virtual Brain (TVB) is an open-source neuroinformatics platform designed to simulate network models of the full brain [28]. It aims to capture and reproduce whole brain dynamics. Using a network-based approach, the brain is represented as a cluster of nodes (representing the neural brain activity) and edges (representing connections between these regions), as seen in Figure 4. The whole-brain network is constrained by i) biologically realistic structural connectivity on a large scale and ii) mesoscopic models that govern the nodes' intrinsic dynamics. The simulation environment allows us to explore neurophysiological mechanisms across different brain scales that generate macroscopic signals. These signals (e.g. functional MRI (fMRI) and EEG) are often used for clinical and research purposes and are therefore suited for applying validation methods against empirical data. Both stereotactic and scalp EEG can be modelled, where we assume the simulated sEEG from TVB are comparable to the recordings measured from the iEEG electrodes from the EANSkE study. Therefore, sEEG simulations from TVB will further be referred to as the simulated iEEG recordings.

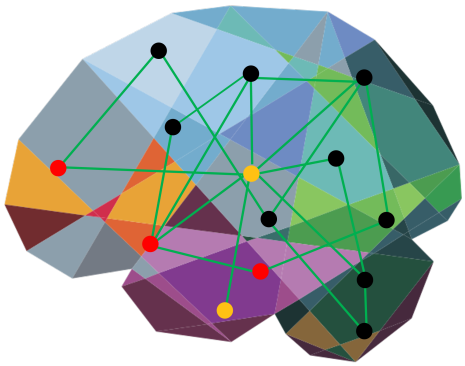

Figure 4: Representation of TVB-setup, where a network-based approach is used by defining functional nodes to govern the dynamics of brain regions which are structurally connected by edges, resulting in a macro-scale model. By varying the node's variables, we can model different scenarios and differ the behaviour between the nodes, illustrated by the different colours of nodes (red, yellow and black).

The connectivity matrix is a key component in realising interaction with the dynamics of the model's network nodes, using specific connection weights and time delays. Diffusion-weighted imaging (DWI) and tractography are obtained to generate this matrix in a patient-specific manner. The result includes a connection weight and tract-length matrix, reflecting the density and physical separation of white matter tracts between nodes, respectively. The latter contributes to the biological realism of the temporal structure of the dynamics. By incorporating individual-specific structural connectivity patterns, the influence of structural differences on functional outcomes can be studied, possibly improving understanding of these mechanisms in patients with neurological disorders.

To obtain patient-personalised large-scale connectivity from neuroimaging data, a processing pipeline tailored for TVB called SCRIPTS can be used [9], [29]. The pipeline uses third-party tools, including FreeSurfer, FSL, remesher and MRtrix, for processing of T1 and dMRI scans [30]–[33]. Using a parcellation template, the brain is divided into several structural regions. This is subsequently used to map the brain's white matter tracts to the structural regions, a process known as tractography, which can be used to develop the connectivity and delay matrices.

Each of the population models that subsequently can be used for representing distinct brain regions is governed by a mathematical model of neural dynamics, simplifying the collective behaviour of neuronal populations. Within the node, we can vary variables and model different scenarios. From here, we can differ the behaviour over the various nodes, illustrated in Figure 4 by the different colours of nodes (red, yellow and black). Biological realism and computational costs balance one another differently, depending on the choice of model. Two-dimensional oscillators, classical population models, such as mean-field models, and multi-modal neural mass models are examples of models with increasing complexity that are available in the TVB framework. The Epileptor model is an example of a neural mass model, characterised by the ability to bifurcate from resting towards a seizure-like state, used in the TVB.

2.2.3 Epileptor model

The brain can be viewed as a high-dimensional dynamical system, defined by a set of system variables which evolve and are governed by dynamical equations and system parameters [12]. The latter is seen as relatively constant. This is not trivial though as, in a biological system, almost all variables change as a function of time. In epilepsy, small perturbations in parameters may induce a transition towards a seizure in susceptible brains. Dynamical models in epilepsy research aim to elucidate these transitions, providing insights into how normal brain functioning shifts towards a seizure. In some cases, this perspective allows us to visualise the brain's behaviour as a bistable landscape, where perturbations can push the system in and out of the seizure state. Other systems use bifurcations to cause system transitions from a non-seizure state to a seizure state, which is described by a gradual change in a system parameter, resulting in a qualitative change in the system's behaviour [34].

The Epileptor model is a mathematical framework specifically designed to capture bifurcation-based dynamics. It provides a simplified, abstract representation of seizure activity that does not focus on the structures that perform the simulated activity but rather on the simulated activity itself. This means that in the case of epilepsy modelling, it models transitions between normal and pathological states. During this project, we use the model based on the Virtual Epileptic Patient (VEP) research of Jirsa *et al.* [9].

Bifurcation theory is a key feature of the Epileptor model for describing transitions from normal to seizure-like states. It can be used to obtain an advanced understanding of the mechanisms during seizure initiation and propagation. The Epileptor can be integrated into large-scale brain network simulations. These properties resulted in the VEP being used in various (clinical) studies involving patient-specific prediction of seizure onset and propagation patterns [9], [35]–[37].

Mathematical framework
The Epileptor model is defined by a set of five differential equations describing two ensembles which operate on different time scales, as seen in Figure 5. Phenomena often observed during seizures are expressed by the fast and slow ensemble, accounting for modelling fast discharges and spike-wave events (SWEs), respectively [34]. The fast discharges are modelled by two state variables x_1 and y_1 that generate an oscillatory behaviour. The SWEs consist of large amplitude spikes followed by long-lasting wave components

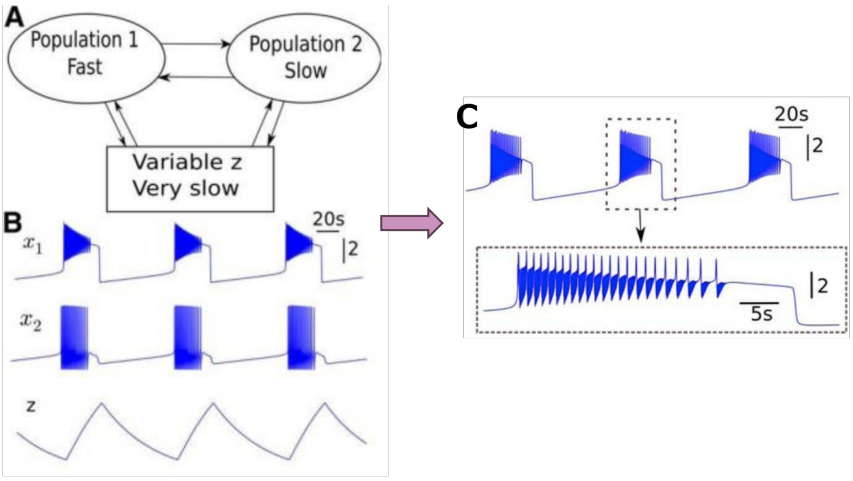

Figure 5: Schematic representation of Epileptor model. (a) The model consists of the interaction of a slow and fast population, which we refer to as an ensemble. Both interact with a very slow z state variable. (b) The fast ensemble captures fast oscillatory discharges during the seizure state. The slow ensemble represents intermediate spike-wave events (SWEs) observed during seizures. Both of them govern two differential equations. A fifth equation is used for a very slow z permittivity state variable. When z crosses a critical threshold, the system abruptly shifts from healthy to seizure-like activity. Similarly, once another threshold is reached, the system returns to a healthy state. (c) The sum of the slow (x_2) and fast (x_1) ensemble defines the local field potential (LFP) of the overall system, which is used to calculate the EEG signal [38].

and are described by two state variables, x_2 and y_2. A fifth equation introduces the permittivity variable (z), orchestrating the transition between a healthy and a seizure state. There is no precise biophysical equivalent of the z variable known and it likely will be complex [9]. The full system is governed by the following set of equations:

$$\dot{x}_1 = y_1 - f_1(x_1, x_2) - z + I_{\text{rest1}} \tag{1}$$

$$\dot{y}_1 = y_0 - 5x_1^2 - y_1 \tag{2}$$

$$\dot{z} = \frac{1}{\tau_0}\left(4(x_1 - x_0) - z\right) \tag{3}$$

$$\dot{x}_2 = -y_2 + x_2 - x_2^3 + I_{\text{rest2}} + 0.002g(x_1) - 0.3(z - 3.5) \tag{4}$$

$$\dot{y}_2 = \frac{1}{\tau_2}\left(-y_2 + f_2(x_1, x_2)\right) \tag{5}$$

where

$$g(x_1) = \int_{t_0}^{t} e^{-\gamma(t-\tau)} x_1(\tau)\, d\tau \tag{6}$$

$$f_1(x_1, x_2) = \begin{cases} x_1^3 - 3x_1^2 & \text{if } x_1 < 0 \\ (x_2 - 0.6(z-4)^2)x_1 & \text{if } x_1 \geq 0 \end{cases} \tag{7}$$

$$f_2(x_1, x_2) = \begin{cases} 0 & \text{if } x_2 < -0.25 \\ 6(x_2 + 0.25) & \text{if } x_2 \geq -0.25 \end{cases} \tag{8}$$

with x_0 = -1.6; y_0 = 1; τ_0 = 2857; τ_1 = 1; τ_2 = 10; I_{rest1} = 3.1; I_{rest2} = 0.45; γ = 0.01. Notably, x_0 controls tissue excitability by serving as a critical parameter controlling tissue excitability. Epileptiform-activity behaviour is generated when above a critical threshold value (x_{0c} = -2.05), while when it remains below, the tissue behaves healthy at all times.

Additional components are introduced to replicate observed dynamics. This involves a linear inhibitory coupling function from the slow to the fast ensemble for the generation of SWEs. A low-pass filtered excitatory coupling function from the fast to the slow ensemble enables the generation of interictal spikes.

Moreover, negative feedback coupling of the permittivity z is added to ensemble 2, influencing the preictal spike density before seizure onset. The time scales ($\tau_0 \gg \tau_2 \gg \tau_1$) of the system allow distinct temporal dynamics of the permittivity variable and ensemble 2 and 1, respectively. It is found that the directed sum of the discharges, -x_1 + x_x, bears an analogy with the field potential, which is why this sum is used to describe the local field potential (LFP) of the model [34]. With that, we can describe the EEG patterns of the full TVB-Epileptor model.

Once we defined the functional node dynamics with the Epileptor, we create a full-head model by coupling multiple nodes. This is achieved with permittivity coupling consisting of a linear difference coupling function and a constant scaling factor. The coupling function integrates local and remote neuronal discharges into the dynamics of permittivity variable z, thereby reflecting the influence of ion homeostatic changes. The scaling factor K_{ij} is a multiplication of the connectome C_{ij} and a constant G. When we consider synchronisation effects only, the signal transmission time delays can be neglected, resulting in the permittivity coupling from area j to area i to read: $\sum_{j=1}^{N} K_{ij} \cdot (x_{1,j} - x1, i)$. Finally, we obtain the full brain model:

$$
\begin{aligned}
\dot{x}_{1,j} &= y_{1,i} - f_1(x_{1,i}, x_{2,i}) - z_i + I_{1,i} \\
\dot{y}_{1,i} &= 1 - 5(x_{1,i})^2 - y_{1,i} \\
\dot{z}_i &= \frac{1}{\tau_0} \left(4(x_1 - x_0) - z_i - \sum_{j=1}^{N} K_{ij} \cdot (x_{1,j} - x_{1,i}) \right) \\
\dot{x}_{2,i} &= -y_{2,i} + x_{2,i} - (x_{2,i})^3 + I_{2,i} + 0.002g(x_{1,i}) - 0.3(z_i - 3.5) \\
\dot{y}_{2,i} &= \frac{1}{\tau_2} \left(-y_{2,i} + f_2(x_{1,i}, x_{2,i}) \right)
\end{aligned}
$$

Assumption of IED-like events
As empirical seizure data is unavailable in this project, we chose to use the Epileptor model to describe IEDs rather than seizure-like events. With this decision, we assume the model is capable of characterising the IED dynamics as what is typically described as the transient events representing seizure-like dynamics.

2.3 Data fitting methods

2.3.1 General overview and challenges

To personalise the TVB-Epileptor model, we need to optimise our parameter set as such to obtain simulations that approach the given patient IED dynamics as closely as possible. One way to overcome this challenge involves parameter estimation by using (real) input data to forecast and quantify the uncertainty of the model parameters, known as inference [39]. A reliable inference method is important to ensure that the finalised parameter set objectively represents the most plausible configuration, given the available data. Preferably, we also want to enable the identification of multiple solutions (if any) to be aware of the different parameter combinations that lead to similar outputs.

Bayesian inference offers a robust framework for this process, supporting the inversion of simulators by identifying parameters that align with both empirical data and prior information. This is formalised in the Bayesian theorem:

$$
p(\theta \mid x) = \frac{p(x \mid \theta)\, p(\theta)}{p(x)}, \tag{9}
$$

where $p(\theta \mid x)$ denotes the posterior probability density of the parameters θ within the mechanistic model, given the observed data x, $p(x \mid \theta)$ is the likelihood of observing data x, given parameters θ, $p(\theta)$ represents the prior distribution over θ, and $p(x)$ is the evidence term. However, in case we don't have the simulator's internal states or real-world experiments are involved, it is often impossible to compute the likelihood $p(x \mid \theta)$ of data x, given parameters θ [40],[41].

2.3.2 Simulation-based inference (SBI)

Simulation-based inference (SBI) refers to a class of statistical methods that estimate model parameters by comparing simulated data to observed data, without requiring an explicit likelihood function [42]. One of the most fundamental forms of SBI is Approximate Bayesian Computation (ABC). ABC is a likelihood-free inference method that is particularly useful for complex, high-dimensional models, such as macro-scale brain simulations .

Instead of directly computing the likelihood, ABC relies on repeatedly simulating data from the model and accepting only parameter settings that produce synthetic data similar to the observed data. Accepted parameters form a set of samples from an approximate posterior. However, these samples do not come from the correct Bayesian posterior. It comes from an approximation based on data, which is centred around the observed data rather than the correctly observed data. The size of variety to which the extension happens depends on the requirement of how similar the accepted synthetic data has to be compared to the observed data, described by threshold value ϵ. Another problem occurs when the number of rejected samples can become so big it becomes practically impossible to match the observed data in case the ϵ-tolerance is decreased [43].

These challenges asked for new methods to be developed involving machine-learning applications of SBI that do not suffer from the same limitations. SBI is based on the development of density estimator architectures (usually a neural network) that enable it to work with both complex high-dimensional observations, e.g. (images and time series) and high-dimensional parameters [40]. SBI can identify the full set of parameter combinations for which the model reproduces the (real) observed data and their corresponding probabilities rather than yielding single solutions only. It can be divided into three main classes: i) neural posterior estimation (NPE), ii) neural likelihood estimation (NLE) and iii) neural likelihood-ratio-estimation. Since we apply the NPE method in this project, we will discuss NPE in greater detail, in addition to the general machine-learning SBI approach.

NPE is characterised to directly target the posterior (Figure 6) [41]. In this type of SBI approach, the neural network is trained with the aim of minimizing the discrepancy between the predicted posterior distribution and the true posterior.

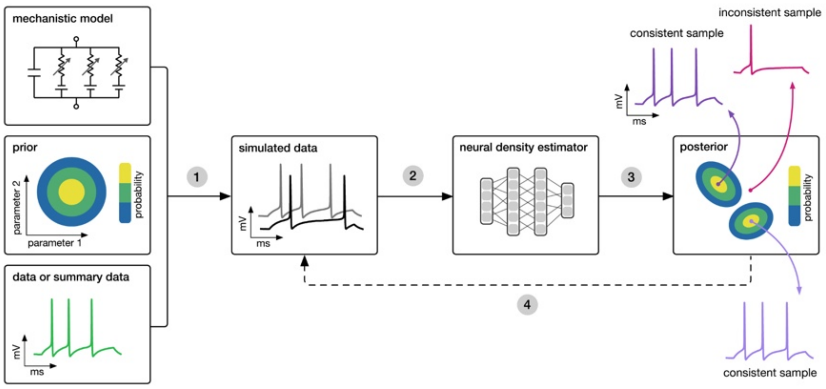

Figure 6: Illustration of the SNPE method, where three inputs are used: a candidate mechanistic model, prior distributions on model parameters, and data (or summary statistics). (1) To proceed, parameters are sampled from the prior and simulated using the mechanistic model. (2) A neural network is trained to learn the association between data and associated parameters. (3) The neural network is applied to empirical (summary) data to derive the posterior distribution. (4) Optionally, an estimate from the posterior can be used for further simulations (referred to as multi-round inference) [44].

Additionally, sequential neural posterior estimation (SNPE) (also known as multi-round inference) aims to effectively refer to the posterior distribution for a particular observation x_o. It initially performs NPE to obtain an initial estimate of the posterior distribution. Then, the previously obtained estimate of the posterior is used for sampling parameters for a new proposal. A new neural density estimator can be obtained by retraining it with respect to the latest proposal. This series of steps is repeated for several

rounds. Although this may reduce computational challenges, it comes at the cost of losing its amortized aspect. Depending on the type of application, either NPE or SNPE may be the most suited alternative. We used both methods during this project. Nevertheless, the final data-fitted model that we will discuss in the methods had been built using the NPE approach only, using the SBI toolbox in a Python 3.11 environment [45].

3 Methods

An overview of the methodology is presented in Figure 7 with the steps taken to develop and analyse the TVB-Epileptor model. In this Chapter, this is explained in more detail.

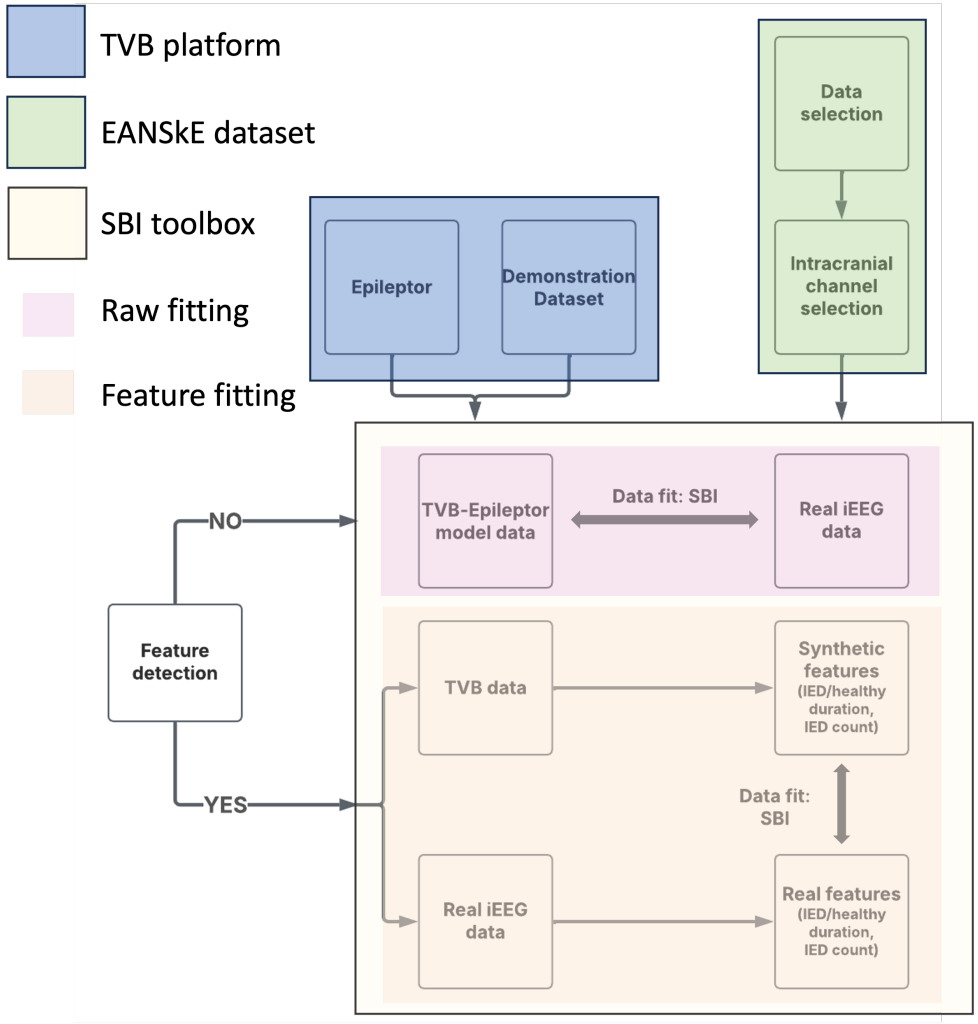

Figure 7: Structural overview of the methodology used. In the TVB platform, the model was obtained using the TVB demonstration connectivity matrices and the Epileptor model (blue box). From the EANSkE study, data was selected considering patients and the desired EEG recordings (green box). SBI was used for a data-fitting strategy (yellow box). Simulations were performed for training two different neural networks based on time-series data (pink box) and 3-dimensional feature-detected arrays (green box). Real data was then fitted in the same structure compared to the trained data from the neural network.

3.1 Data selection and processing

The most important criterion during patient selection was the availability of iEEG data, where the recordings show visually detectable IEDs. Scalp EEG data was discarded for now. Two patients were included, further referred to as Patient A and Patient B. Patient A was selected for initial analysis. To increase the robustness of the findings, Patient B was incorporated later. This dataset included a high number of IED events with diverse temporal characteristics, making it particularly valuable for modelling IED patterns.

For both Patient A (one recording) and Patient B (two recordings), we included recordings of lengths between 25 and 35 minutes. EEG recordings were sampled at 250 Hz. Afterwards, it was annotated by a clinical expert on both IED observed patterns and (EMG) artefacts, using mainly the scalp EEG

channels. Subsequently, EEG signals were normalised (by centring it towards a mean value of 1 and variance of 1) to ensure consistent variance and avoid bias in further analysis.

Before proceeding with data-fitting procedures, we reevaluated the annotated IEDs in MATLAB with a focus on the iEEG channels. Where discrepancies in duration between scalp and intracranial EEG existed, adjustments were made. The start and end points of the IEDs were identified as the earliest and latest instances of IED characteristics observable across any iEEG channel. Some annotated IEDs contained prolonged durations (e.g. over 30 seconds). Typically these intervals could be divided into smaller intervals, separated by short healthy intervals. To qualify a short healthy intermediate interval, a complete recovery of frequency and amplitude behaviour had to be observed across all channels. Once all IED annotations were checked, sample counts were saved as an IED duration feature for further analysis. Unlike Patient A, for Patient B MRI scans before and after DBS implantation were not available. Initially, we considered the MRI dataset to be an inclusion criterion as well for personalised structural connectivity purposes. Besides, this could allow us to determine the precise location of the electrodes in the ANT. However, as this step towards model personalisation has not been performed yet, we could neglect this criterion for now.

3.2 Computational modelling

We used the TVB platform for developing the computational model (v2.7.2, see http://www.thevirtualbrain.org). Ideally, personalised connectivity matrices derived from DTI and fMRI data would have been used for structural connectivity identification. However, due to practical and time constraints, the default demonstration dataset provided by the TVB platform served as a sufficient substitute, providing a network consisting of 76 nodes. Three nodes per hemisphere are located in the subcortical area, representing the hippocampus, parahippocampus and amygdala areas. Notably, the thalamus (and thus the ANT) region is not included. The connectivity matrices provided by TVB, representing the weight and tract length values between all regions, can be seen in Figure 8. With weight and tract length values, the connections between regions are classified by strength and delay of signal transmission, respectively.

Then, we used the Epileptor, a neural mass model able to reproduce epileptiform dynamics, for implementation across the 76 nodes using Python (v3.11.8) [34]. As explained in Chapter 2.2.3, we use the Epileptor to describe IED events rather than seizure-like events. The model comprises five state variables acting on three different time scales. The system exhibits fast oscillations and spike-wave behaviour during an IED-like state through the two faster time scales. The slowest time scale, referred to as the slow permittivity coupling state-variable z, accounts for autonomous switching between healthy and IED-like states through saddle-node and homoclinic bifurcation mechanisms for the seizure onset and termination, respectively. When we have no network coupling (i.e. when the Epileptor is in isolation), and the neural mass is above threshold $x_0 > x_{0,C}$, the Epileptor can trigger epileptiform dynamics. Inversely, if $x_0 < x_{0,C}$, the Epileptor does not trigger any epileptiform behaviour. In our model, we assigned only one node to exceed the threshold $x_{0c} = 2.05$. The nodes were connected via permittivity coupling, acting on the z state-variable. We assigned additive white Gaussian noise (mean 0, variance 0.0003) to the state variables x_2 and y_2 to capture stochasticity. The stochastic Heun integration method is used to solve the model over time, using a 0.05-second step size, based on values found in literature [9]. These design choices allowed simulations that captured epilepsy-specific patterns while we could maintain computational feasibility in data-fitting methods described subsequently.

3.2.1 Channel selection

To compare model outputs with real EEG data, we prioritised the selection of iEEG channels to minimise the effects of attenuation artefacts. Signal attenuation can result from various factors, such as the propagation of signals through tissue layers with varying conductivity or geometric simplifications in the modelled head structure. Also, in TVB simulations, the signal is affected by parameters such as tissue conductivity, numerical resolution and geometry of the head model. Signals originating in deeper brain structures thus have a higher probability of appearing diminished or distorted, particularly when measured at the scalp level.

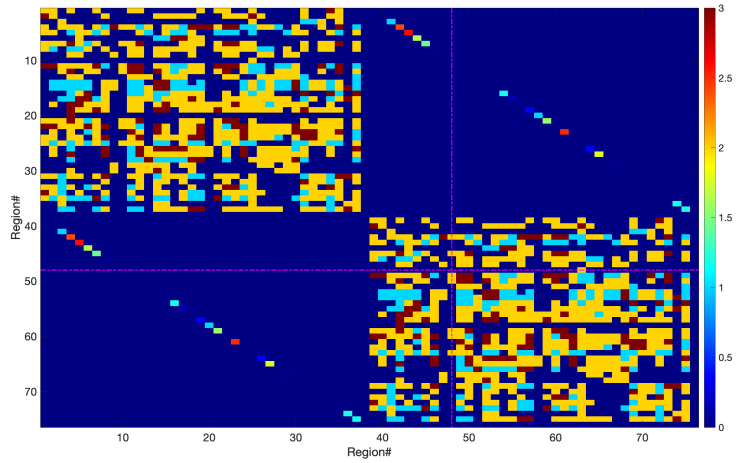

(a)

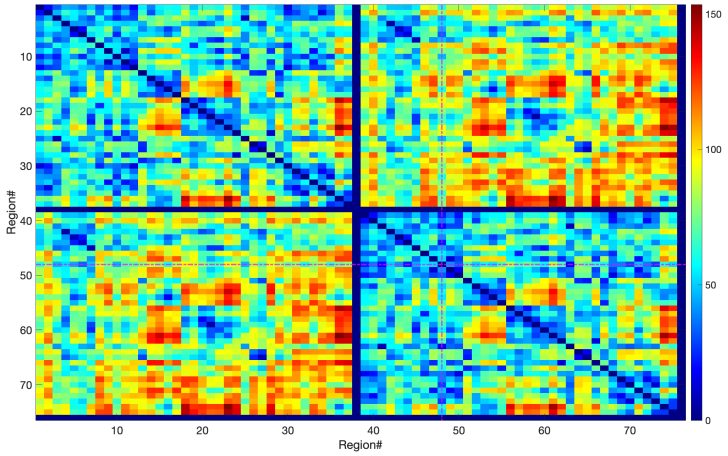

(b)

Figure 8: Connectivity matrices of (a) weight and (b) tract length provided by the TVB 76-region demonstration dataset. The dashed horizontal and vertical lines indicate the connectivity values from and towards the left hippocampus, respectively. Self-connections are represented on the diagonal.

To address this, we selected eight from the 588 iEEG channels provided in the TVB. The channels were located in the subcortical area and placed symmetrically over the two hemispheres to mirror the setup of the real experiments. Furthermore, channels were included only when the raw time-series data of the simulation displayed a clear visual difference between the healthy and IED-like states.

3.2.2 Simulation processing

During simulation, the LFP of all nodes (directed sum of the state variables, $-x_1 + x_2$), permittivity state variable z, and the iEEG are saved for further processing. All signals were saved at a 256 Hz sampling frequency.

To prepare the data, transient behaviour was removed by discarding the first 5 seconds of the simulation. Normalisation was then executed by subtracting the mean and scaling the variance to 1. During data-fitting procedures, this avoided the influence of scaling difference effects between the real and the synthetic signal.

For the iEEG signal, we changed the montage of the eight selected channels into three left and three right bipolar montages, which were subsequently stacked into one array for further analysis. These processing steps (including sampling frequency, data normalisation, and bipolar montage) were chosen to closely replicate the real measurement setup. The resulting stacked iEEG array served as the synthetic raw time signal for upcoming purposes concerning data fitting.

3.2.3 Feature extraction

After processing the time-series simulations, we wanted to extract the IED duration, IED count and healthy duration, and use these as features for data fitting. For this, we used the z state variable due to its triangular wave-like behaviour, capturing the transition between IED and healthy state. The procedure used for this starts by detecting the peaks and valleys of the z state-variable time series, with a minimal peak prominence of 0.2. The valleys in the z variable correspond to the bifurcation to the IED state of the system, whereas the peaks mark the termination of this state. Then, the IED duration is calculated as the difference in time index between the subsequent peaks for each valley. To ensure accuracy, we included only complete IEDs—intervals that both began and ended within the simulation period. Incomplete IEDs (e.g., those starting before t = 0 or ending after simulation termination) were excluded to prevent skewing the calculation of average IED duration, the first feature. The second feature, IED count, was defined as the total number of complete IED events within the simulation. The third and last feature includes the healthy duration of the signal. Here, we prefer to consider the complete time the system remained in its healthy state, as we are only interested in the cumulative healthy duration. We determine this by summing the intervals where the signal exhibited a negative slope.

An example of the feature detection procedure is given in Figure 9. It shows a total of three IED occurrences within the interval, with the first two being identified as complete events. The detected IED interval is visualised by the blue dashed line, with the corresponding duration in milliseconds. The initiation and termination of the IED interval are indicated by the green and red marked dots, respectively. The remaining healthy signal is indicated by the solid red line. Finally, the original z variable which is neither marked as an IED interval nor as a healthy interval, is given in grey during the approximate last second of the simulation.

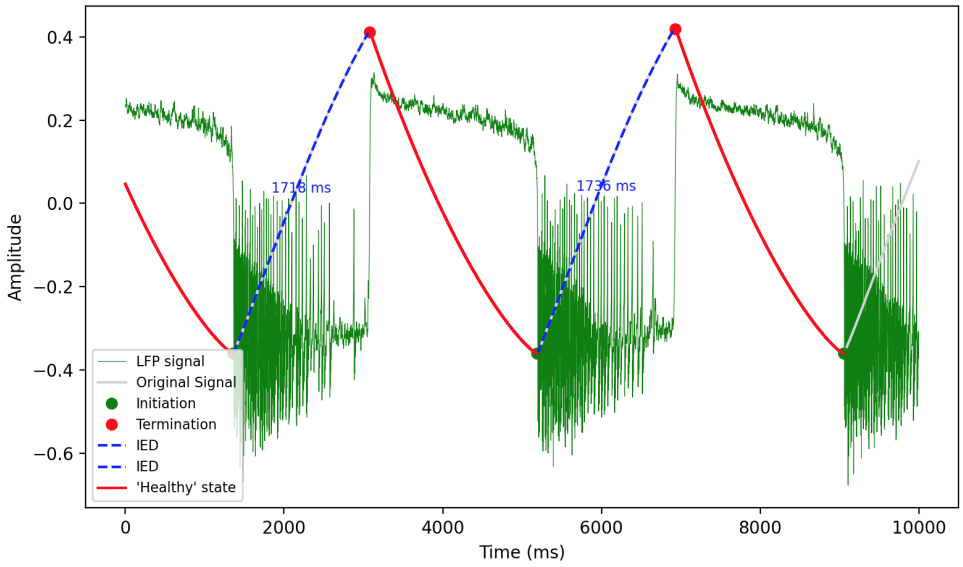

Figure 9: Example of the feature detection approach using the linear oscillatory z state-variable. We observe the detection of two complete intervals of an IED (dashed blue line) followed by a healthy interval (solid red line), where each IED-state duration is given in ms. The IED duration is then calculated as the mean duration of the two IED intervals. Initially, the system is in its healthy state, and duration is found by summing all intervals where the signal exhibits a negative slope. The green line corresponds to the associated LFP signal of the node model, showing a change in mean signal value with oscillatory behaviour in the IED-like state. Initiation and termination of the IED-like state are marked by the green and red dots, respectively.

3.3 Simulation-based inference

Once we completed the real data processing, setup of the computational model and synthetic data selection, we implemented SBI in three stages.

- *Synthetic data fitting* was applied, by simulating data of the TVB-Epileptor model with known

reference parameter values. This stage allowed the evaluation of the SBI setup and its convergence behaviour with an increasing number of simulations, particularly for high-dimensional data.

- We used the same network to infer parameter distributions for real patient iEEG recordings for *real data fitting*. The purpose was to investigate whether SBI enabled parameter estimation that aligns more closely to the real EEG data characteristics (discussed in more detail in Chapter 3.3.2).
- *Real data fitting* was extended by fitting specific features of the time signal only. This corresponds to the 3-dimensional feature array (IED duration, IED count, healthy duration).

These design choices will be elaborated after describing the general SBI methodology.

As a first step towards obtaining posterior distributions for the varied parameters, we sampled parameter configurations uniformly across their predefined ranges (named priors), as provided in the TVB Epileptor source code. Fixed parameters were assigned their default values, shown in Table 1. Not all parameters could be varied due to computational costs. We selected parameters by visual inspection of epileptiform behaviour during simulation (e.g. initiation and termination patterns and changes in IED state) with individual parameter variation and by referencing existing literature [46].

Next, we performed a series of simulations for all sampled parameter configurations using the computational model to generate training data. Both the high-dimensional raw iEEG signals and the extracted IED duration features were used as input for the SBI toolbox. With this, we generate two distinct neural networks; one trained with time-series-based data and one trained with feature-based data. The parameter configurations were randomly sampled from the same uniform-distributed prior parameter distributions [45]. Specifically, this was done via Neural Posterior Estimation (NPE) [41]. Here we directly target the posterior distribution of the model parameters given the observed data. It trains a neural network to map simulated data to their corresponding parameters, without requiring an explicit likelihood function.

We obtained the relative posterior probability distributions by sampling the trained neural networks for all IED observations. The posteriors were smoothened and visualised in one figure using kernel density estimation (KDE) for individual parameters on the diagonal and pair plots on the upper triangle to assess inter-parameter relationships. Important informative characteristics of the relative distributions to note are the overall shape and peak locations, rather than absolute probability values. In all cases, 1000 samples were used. The maximal posterior could be determined and visualised with the toolbox for further evaluation. This involved comparing the distributions against ground truth values known from synthetic data, as well as observed features (either raw time signals or IED durations) extracted from real patient data.

Table 1: Parameter values for the TVB-Epileptor model.

Parameter	**Meaning**	**Range/ fixed value**	**Reference value**
x_0	Threshold for ability epileptiform-activity generation.	[-2.05, -1.0]	-1.6
K_s	Permittivity coupling from intermediate to slow time scale.	[-4.0, 4.0]	-0.2
r	Temporal scaling in the z state variable.	[0.0, 0.001]	0.00015
K_f	Coupling scaling on the intermediate time scale.	0.1	
I_{ext_1}	External stimulus to the first ensemble.	3.1	
I_{ext_2}	External stimulus to the second ensemble.	0.45	
slope	Linear coefficient in x_1 state variable.	0.0	
K_{vf}	Coupling scaling on the fast ensemble.	0.0	
tt	Time scaling of the whole system.	1.0	
τ_2	Temporal scaling coefficient in y_2.	10	

3.3.1 Synthetic data fitting

The simulated signal length was based on the IED segments recorded from Patient A's database, yielding a 7506-dimensional signal (6 channels with a 1251 sample length, corresponding to approximately 4.89 seconds). The number of simulations varied between 750 and 51,000. By visually inspecting the posterior distributions, we compared the obtained estimates with the reference parameter values (given in Table 1).

3.3.2 Real data fitting

Time series fitting
For real data fitting of the raw time series, only the recording of Patient A was used. The iEEG data served as input for the trained neural network during synthetic data fitting. Before visualizing the data-fitted model, we checked convergency characteristics. An important criterion for this included assessing whether the distribution could be characterised as narrow. A narrower posterior indicates greater certainty in the estimated parameter values, whereas a broader posterior suggests higher uncertainty or insufficient data to constrain the model sufficiently. Ideally, we observe Gaussian-like symmetry characteristics. Additional checks therefore also included identifying the presence of multiple peaks and the occurrence of convergency towards domain boundaries, indicating issues with prior domains or limitations in the model performance.

Key features for real and synthetic comparison included a) change in amplitude from the healthy to IED interval, b) IED duration, c) healthy and IED count content and d) morphology (e.g. exhibiting spike-wave-like features). This is based on literature and visual inspection from experts [19].

Feature fitting
We used both datasets of Patient A and Patient B for the feature-based fitting analysis. While data of Patient A were limited to short IED lengths, Patient B offered more IED events. A simulation length of approximately 5 seconds could not suffice anymore, as part of the dataset contained longer measured IED durations and 15-second simulations were introduced additionally.

After simulations, we used the z state variable of the model for feature detection, generating a 3-dimensional signal per simulation capturing the IED and healthy duration and IED count (as described in Chapter 3.2.3).

We performed 50,000 simulations, similar to the previously used amount for time-based neural network training. This choice balances the need for sufficient training data with the increased likelihood of invalid simulations. This can arise for two main reasons. Firstly, some parameter sets from the prior may lead to unstable model behaviour, affecting both time-series-based and feature-based neural networks. Secondly, invalid simulations may also arise if no IED is detected in the simulation, making feature extraction impossible. The latter will only affect the feature-based neural network. Despite this additional possibility of invalid simulations, we did not expect the need for additional simulations. This is because the feature-based neural network operates on reduced-dimensional data, requiring fewer simulations for convergence compared to the higher-dimensional time-series-based network.

For sampling the posterior, we processed and transformed the real IEDs to match the synthetic format. After finishing the IED detection procedure (Chapter 3.1), the IED duration was calculated by transforming the unit from seconds to samples. Knowing the total duration, the healthy duration could be directly calculated from this. Lastly, we fixed an IED count value for all real feature arrays at 1, to ensure a single IED per simulation.

4 Results

4.1 Data selection and processing

An example of the available dataset containing an IED signal of both Patient A and Patient B is illustrated in Figure 10. The top six channels represent intracranial measured signals while the bottom channels show the simultaneous measured ECG. In Figure 10a, the signal alters which can be identified as an IED that starts around 412 seconds, with an approximate 1.70-second duration. In Figure 10b, an IED starts around 276 seconds, with an approximate 3.30-second duration. These events are characterised by a change in amplitude and a disruption of the background activity.

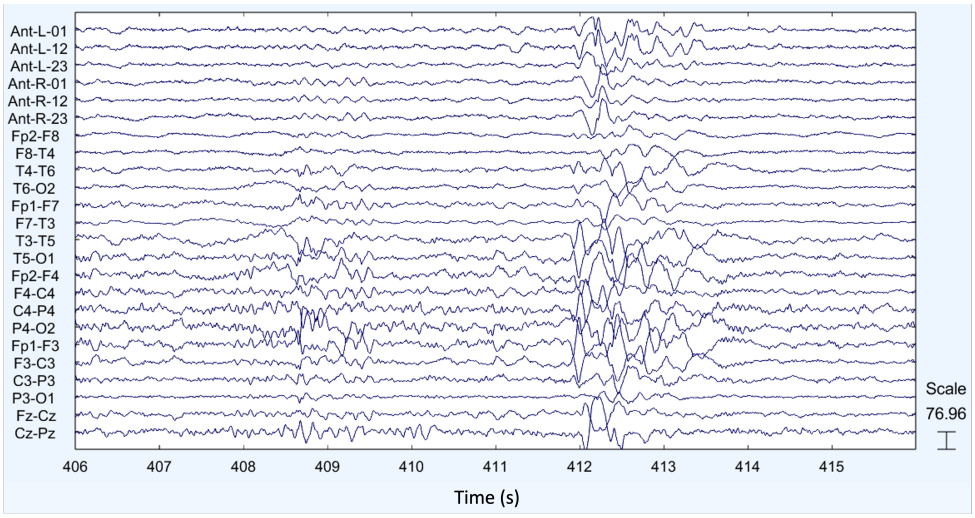

(a)

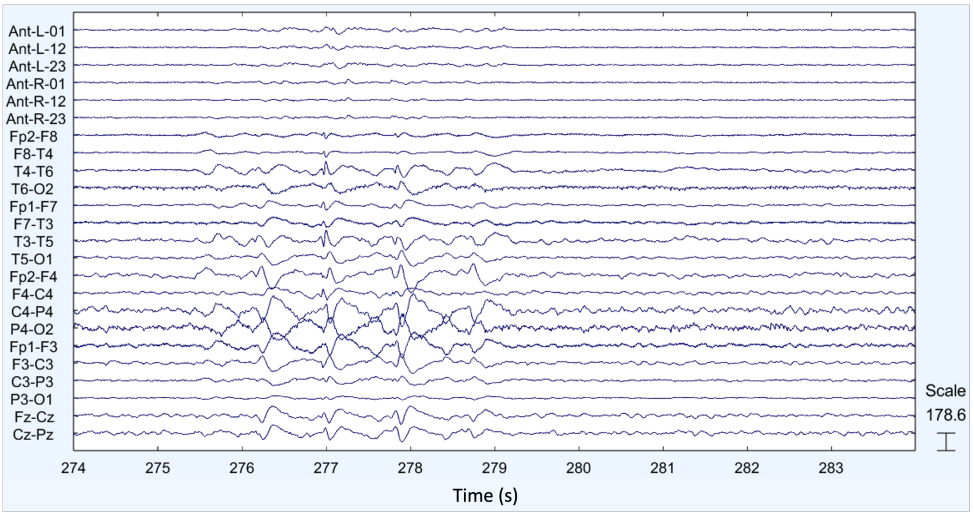

(b)

Figure 10: Example of raw time-series recordings capturing for both Patient A and Patient B. The top six channels represent iEEG montages, while the remaining signals display different scalp EEG montages. (a) An IED is observed starting around 412 seconds, with an approximate 1.70-second duration. (b) An IED is observed starting around 276 seconds, with an approximate 3.30-second duration.

In Patient A's EEG dataset, a total of four IEDs were observed. In contrast, the dataset for Patient B exhibited a higher count, with 140 IEDs detected across two measurements. The distribution of the IED durations for Patient B is visualised in Figure 11. It illustrates a histogram alongside its corresponding kernel density estimation (KDE). The majority of the IEDs have a duration between 0.5 and 5.0 seconds. However, also longer durations are observed, approximately up to 14.0 seconds.

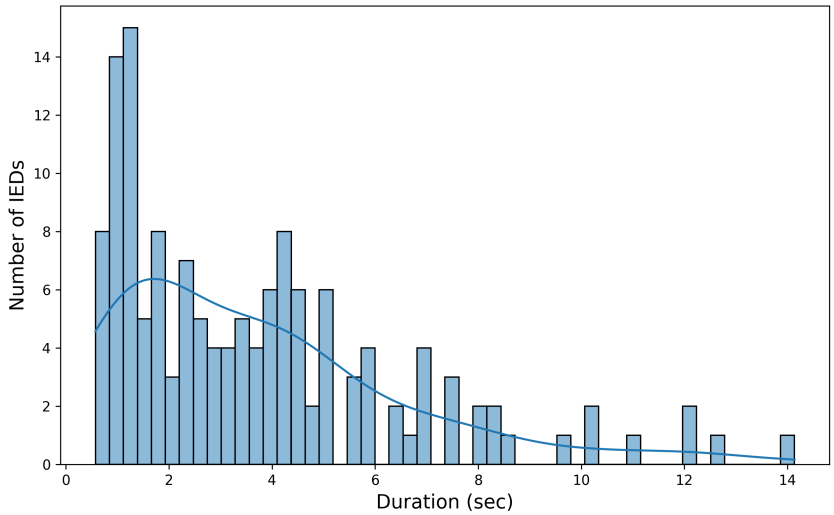

Figure 11: Distribution of the annotated IED durations from Patient B with the corresponding kernel density estimation (blue line). Most IEDs have a duration in the range from 0.5 to approximately 5.0 seconds.

4.2 Computational modelling

4.2.1 Node and channel selection

Among six potential subcortical nodes (i.e., hippocampus, parahippocampus, and amygdala in both hemispheres), the left hippocampus was selected as the node generating epileptiform activity. This choice was based on trial and error testing, ensuring the stability of the model and reproducibility of simulated IED-like activity for varying parameter configurations.

The channels were chosen based on the requirement described in Chapter 3.2.1, accounting for symmetrical and subcortical placement and visibility of IED-like behaviour in the time-series output. The final head model with the anatomical node markers, selected epileptiform-active node marker, and recording channel markers can be seen in Figure 12.

4.2.2 Feature extraction

We processed the identified IEDs to extract their key features, forming the foundation for subsequent data-fitting methods. Feature detection accuracy was carefully inspected, with most cases correctly identified, as illustrated in Chapter 3.2.3, Figure 9. Additional examples are provided in Appendix B. However, a few deviations from expected detections were observed. We can classify these inconsistencies into six different types (Figure 13).

Figure 13a shows an example of a scenario where no IED is detected. The z state variable initially enters a transient phase and stabilizes after approximately three seconds, remaining flat thereafter, leading to the absence of IED detection. While most of the signal is classified as healthy, a portion is identified as neither IED nor healthy. We expected the whole signal to be classified as healthy beforehand. This however will not influence further analysis as no IED detection will return NaN values for both the IED duration and IED count.

In Figure 13b, we observe an IED that has not yet been completed and therefore not identified as an IED. This is indicated by the grey line, rather than the dashed blue line for detection. We made this design choice to avoid unreliable results of the corresponding captured IED duration. In total, this occurred 16 times.

In Figure 13c, a new IED initiates within the simulated interval but does not fully complete. As a result, the algorithm does not count it as an IED, similar to the first scenario. While SBI may still identify a close parameter match, its accuracy is limited, as only one IED should initiate per interval. This behaviour was observed three times in the combined dataset from Patient A and Patient B.

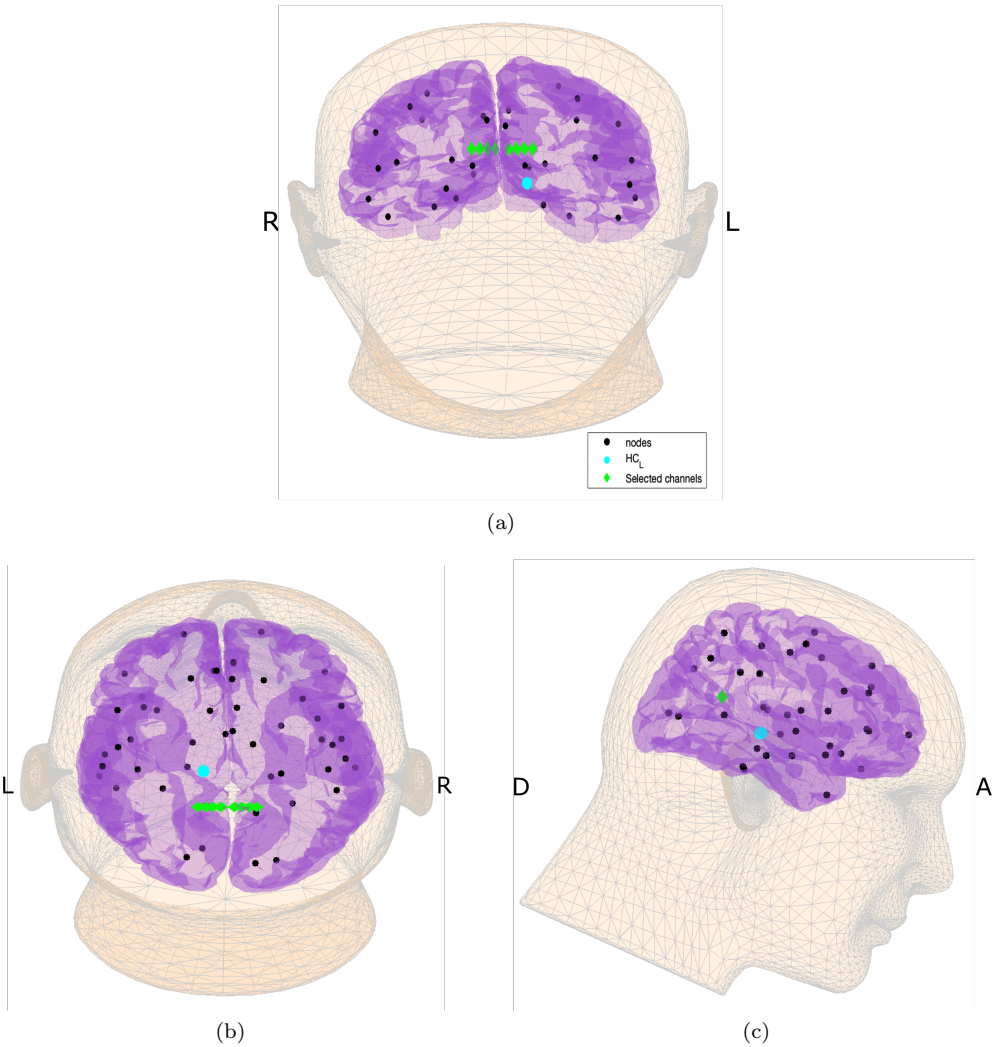

(a)

(b)

(c)

Figure 12: The head model used in the TVB-Epileptor simulations is shown in the 3D view from three perspectives: (a) coronal, (b) axial, and (c) sagittal. Healthy nodes with predefined parameter configurations are marked in black, whereas the epileptiform-active node is seen in blue (HC_L). Selected channels for iEEG measuring are marked green.

Some IEDs were neither identified nor classified as healthy behaviour, as seen in Figure 13d. This rare issue, occurring only once across all patients and neural networks, is linked to the transient behaviour of the z state variable in the first two seconds of the simulation.

For some parameter configurations, the z state variable shows completely unexpected behaviour, as illustrated in Figures 13e and 13f. In Figure 13e, many local maxima are detected and counted as IED-to-healthy transitions or vice versa. However, there is no constant oscillation of the z state variable at all. In Figure 13f, we observe a damped sinusoidal system. In both cases, the corresponding LFP signals (plotted in green) show no visual transition from one state to another as is typically seen in the Epileptor model. These types of behaviour depicted by Figures 13e and 13f were seen twice and once, respectively.

Despite the inconsistencies, we expect their impact on further data-fitting analysis to be small, as correct feature detection occurred dominantly. Therefore, we expect the neural network training will not have been affected to a great extent.

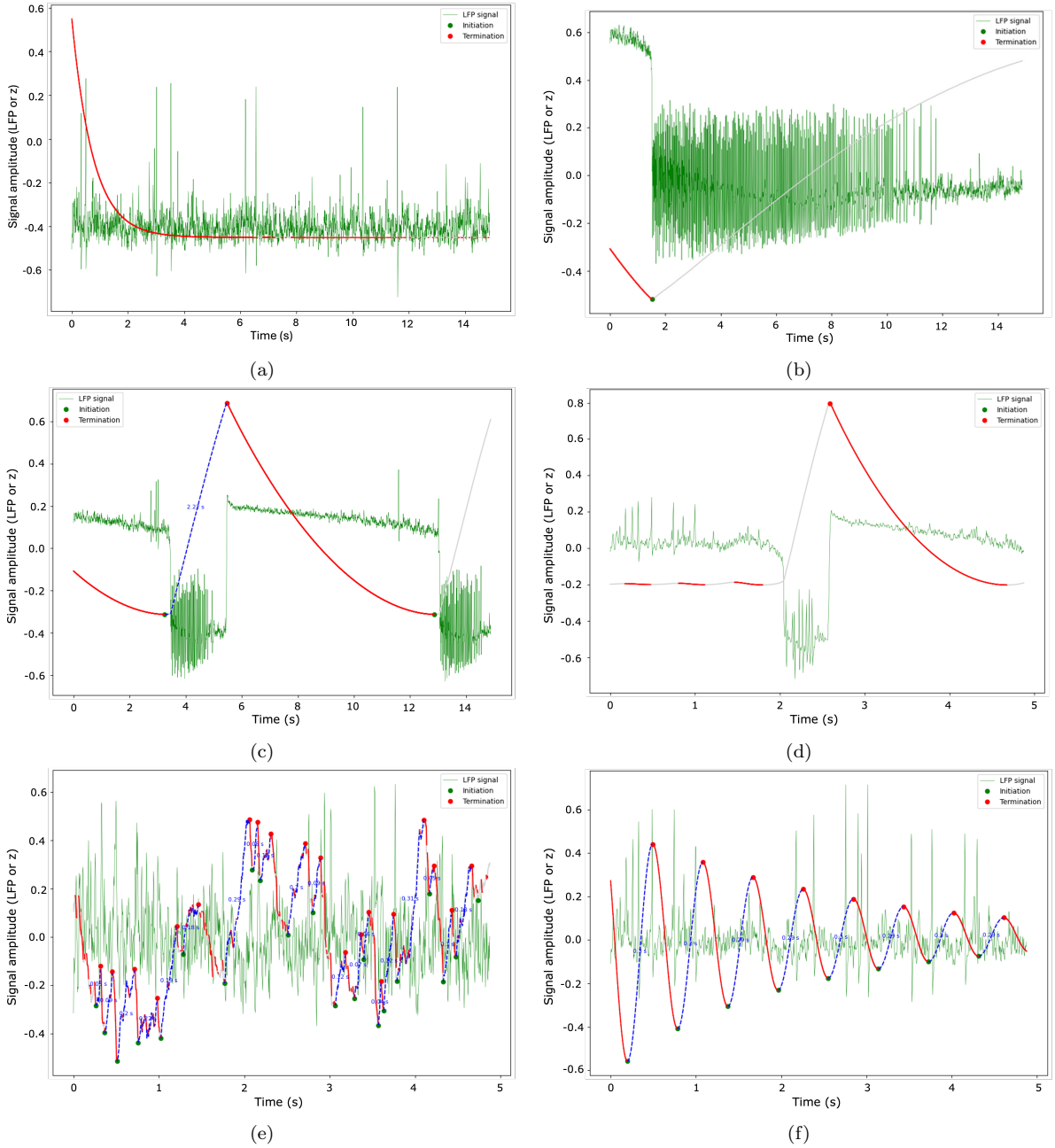

Figure 13: Different types of feature detection inconsistencies, seen in 5-second or 15-second simulations. The z state variable, responsible for detecting both healthy and IED behaviour, is plotted in grey and marked in red and blue (dashed line) for detected healthy and IED behaviour, respectively. In green, the corresponding LFP signal is illustrated. The onset and termination of the IED state are depicted with the green and red dots, respectively. (a) Example of the scenario where no IED is detected. The z state variable starts in its transient state. After approximately three seconds, it remains flat, resulting in no IED being detected. The majority of the signal is detected as healthy, but some is detected neither as IED, nor as healthy. (b) An example of an incomplete IED, which is thus not detected. (c) The initiation of a second IED, already occurring in the interval. However, as the IED is not finished, it is not detected by the algorithm. (d) A complete IED halfway through the simulation is missed. (e) A complete lack of oscillatory behaviour of the z state variable. Instead, we observe a noisy signal. (f) Rather than linear oscillations, we observe a damped sinusoidal system without visual state transitions in the corresponding LFP signal.

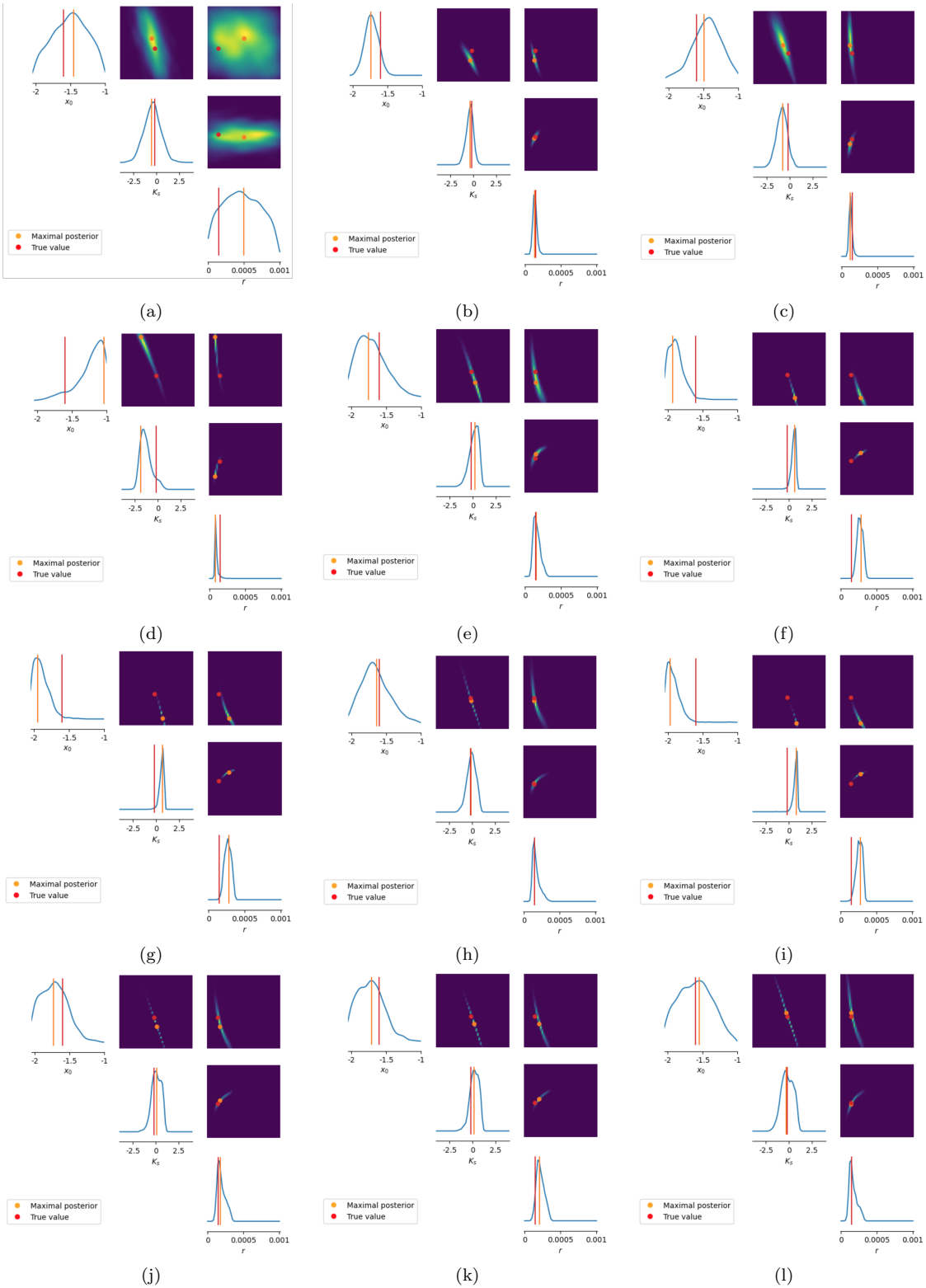

Figure 14: Relative probability distribution posteriors were sampled with synthetic raw data from SBI-based trained neural networks. The neural networks are built with an increasing number of simulations, starting with 750 simulations (a) and up to 50250 simulations (i), in steps of 4500 simulations. The maximal estimated probabilities (orange) and constant ground truth values (red) for x_0, K_s, and K_f are given in both 1- and 2-dimensional domains on the diagonal and upper triangle, respectively.

4.3 Simulation-based inference

4.3.1 Synthetic data fitting

The results of synthetic data fitting confirm that SBI refines parameter estimates as the number of simulations increases. The evolution of the relative probability density distribution characteristics of x_0, K_s and r for increasing number of simulations towards the reference dataset is presented in Figure 14. The SBI-estimated maximal posterior values (orange) and reference values (red) are marked for comparison. When we observe the evolution of the orange line for the increasing number of simulations, we generally notice the difference between the SBI-estimated and reference values reduces for all three parameters as aimed for. Moreover, the three parameters show single-peaked probability functions regardless of the applied number of simulations. However, variations are evident in the distribution shape, especially for parameter x_0. This is caused by i) the differences between more narrow and broad distributions and ii) the location of the maximal probability values over the different number of simulations. For x_0, we see that the maximal posterior starts in the centre of the domain (close to its reference value). Then, it converges to the right boundary (Figure 14d) followed by a similar transition to the left boundary (Figure 14f and g). After this, the probability function returns to the centre of the domain and broadens again. In contrast, parameters K_s and r exhibit more stable convergence, with the maximal posterior values remaining relatively consistent. Also, their distributions become more concentrated as the number of simulations increases, where no parameters approach the domain boundaries as closely as x_0.

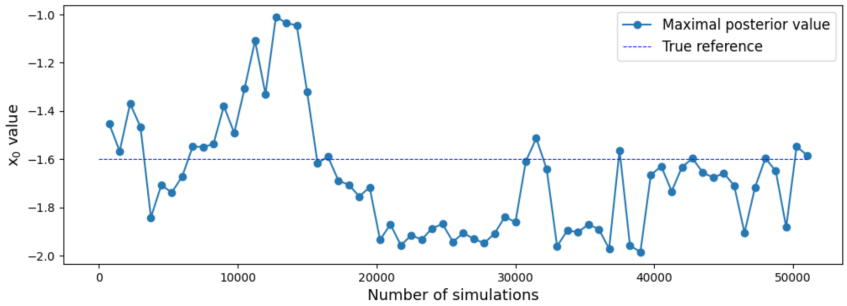

(a)

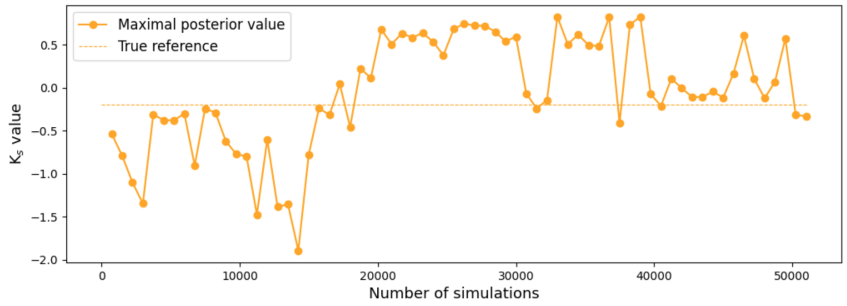

(b)

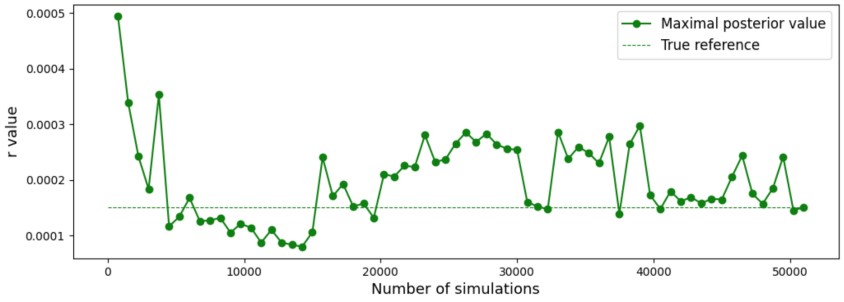

(c)

Figure 15: Parameter values found by maximal posterior estimation from the SBI neural network against an increasing number of simulations for a) x_0, b) K_s and c) r, plotted as solid lines. The dashed line depicts the reference value for each parameter.

In Figure 15, we notice the differences between the SBI maximal posterior estimated values (solid line) and the reference values (dashed line) of the three parameters x_0, Ks and r, for increasing number of simulations and 750 simulations as step size. For all three parameters, the error initially decreases, with a pronounced drop around 16,000 simulations. However, before this, parameters x_0 and K_s experienced a temporary increase in error compared to the initial estimates at 750 simulations. Beyond 16,000 simulations, the difference stabilises, with the SBI estimations fluctuating around a relatively constant level. This fluctuating difference for K_s and r is for almost all different numbers of simulations a positive difference (indicating the SBI-estimation values are higher than the reference), whereas for x_0 it is negative. Importantly, the error does not consistently approach zero.

In the final probability distributions based on 51,000 simulations (Figure 16a), the SBI-derived configuration is closely aligned with the reference values of all three parameters. Using this maximal posterior configuration, we compared the two synthetic datasets from the reference and SBI-based parameter configurations by overlapping their time series in Figure 16b. The result shows the SBI-estimated simulation in red is visually mostly similar to the reference simulation (grey), as we observe an identical overlap in the majority of the interval. However, a small time shift occurs when the system bifurcates towards the IED-like state, and similarly when the system bifurcates back to a healthy state. Moreover, when comparing it to Figure 10, we observe that the simulated data differ from the real data. For instance, the dominant frequency of the TVB-Epileptor model is higher, during healthy and unhealthy intervals. Furthermore, instead of a change in amplitude with a constant mean value of the signal for the IED interval, we observe a change in the mean value of the signal between approximately 1 and 2.6 seconds.

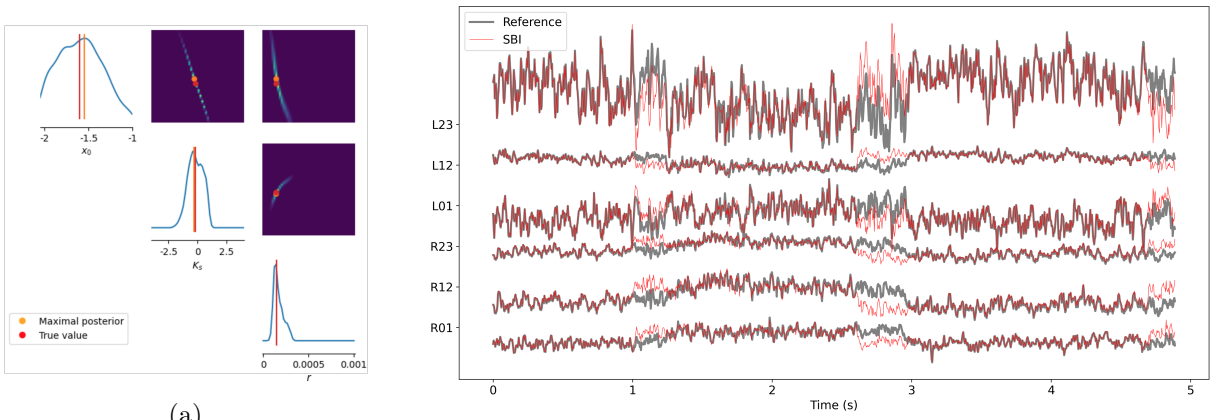

(a) (b)

Figure 16: SBI results of synthetic data fitting after neural-network training based on 51,000 simulations. (a) Probability distributions for each parameter, with the SBI-estimated maximum posterior value shown in orange and the reference values in red. (b) Comparison of time-series simulations, where the reference signal (grey) is overlaid by the SBI-estimated signal (red) across all six montages. We observe a shift of IED interval, with the SBI-estimated simulation bifurcating earlier into and out of the IED-like state.

4.3.2 Real data fitting

Once synthetic data fitting was applied, we fitted the real data based on two different neural networks. First, we used the same neural network trained with time series resulting from the synthetic data fitting. Then, we extended fitting the real data by fitting specific features of the time signal only. The IED duration, IED count and healthy duration were chosen for this.

Time series fitting

Figure 17 illustrates the results of fitting the raw time series for one of the four IEDs of Patient A. Figure 17a includes the posterior distribution, in which the narrow peaks indicate a convergence of the single-peaked distributions. The three orange-marked values indicate the parameter configuration used in the simulations, of which the results are shown in Figure 17b, for one synthetic channel with the corresponding real channel, and Figure 17c, for all synthetic channels. The IED-like and healthy behaviour in the TVB-Epileptor model show similar characteristics compared to earlier observations. We see a dominant high-frequency component in the whole time interval and a change in mean value between 3.2

and 4.0 seconds corresponding to the IED-interval (indicated in Figure 17b as the orange highlighted area). The real IED is annotated as the blue-marked period in Figure 17b between 1.2 and 4.2 seconds. Here, the normal background activity is disturbed by a change in amplitude. Frequency and amplitude characteristics within the simulated IED and healthy intervals do not resemble the real signal, mirroring observation seen in Chapter 4.3.1. This is also highlighted by the observation of the timing and duration mismatch between the two signals of the IED interval. Similar characteristics are observed for the three remaining IEDs of Patient A, which can be found in the Appendix C.

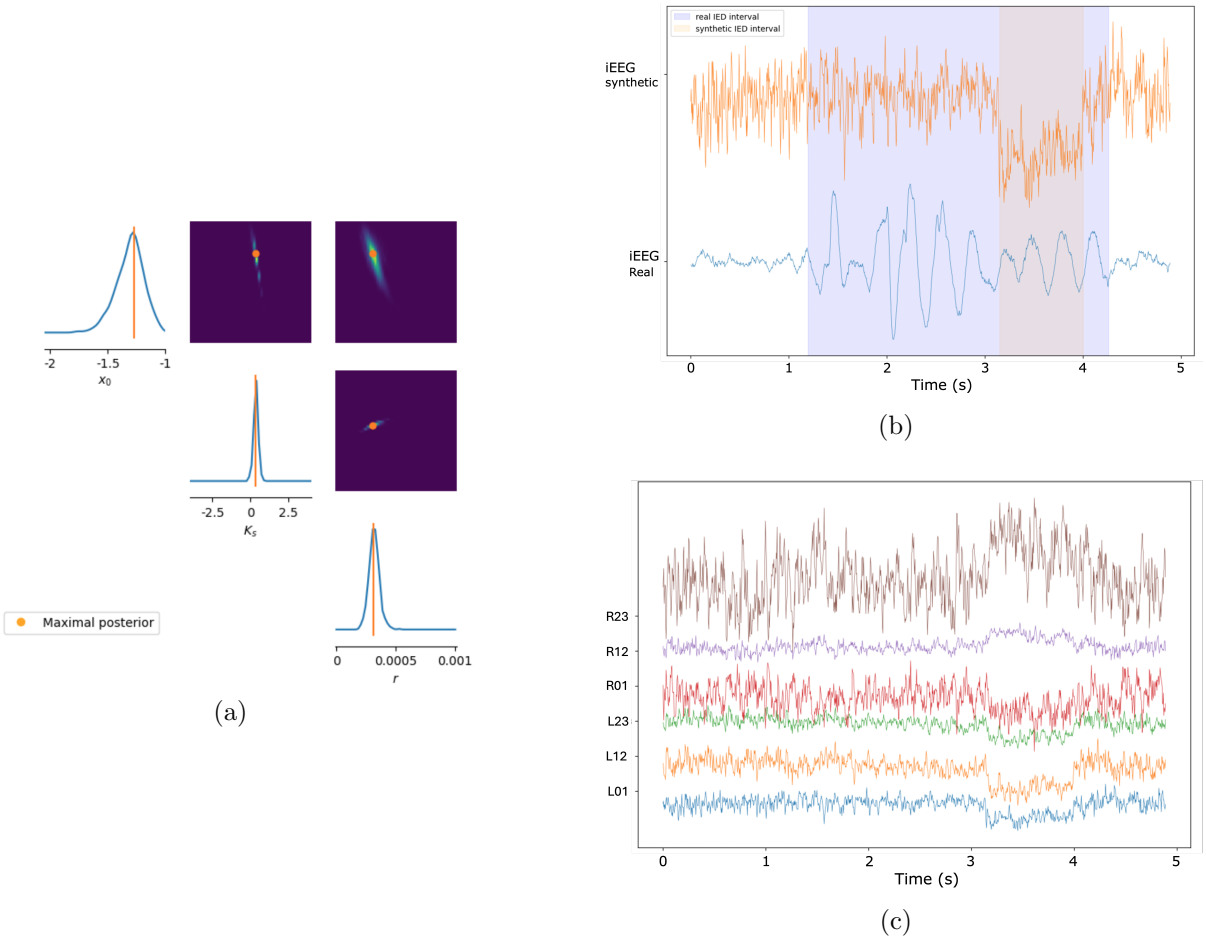

Figure 17: Results of SBI real whole time series data fitting in one the IEDs in Patient A. (a) The SBI posterior after 51,000 simulations with the maximal estimated posterior marked in orange. (b) Synthetic SBI-estimated channel and real channel plotted against time, which is in both cases the R01 channel. The blue and orange marked intervals indicate the real annotated and SBI-estimated IED interval, respectively. (c) All synthetic iEEG channels from the SBI-estimated parameter set.

Feature fitting

For Patient A, we examined the SBI estimated features using neural networks trained on both 5-second and 15-second simulations. The latter was introduced additionally as part of the dataset of Patient B, which contained longer annotated IED durations. In particular, the 5-second based neural network produced SBI-estimated features with small differences compared to the real value, as summarised in Table 2. All IEDs were replicated once in the interval, reflecting the real IED count feature. IEDs 1, 2 and 4 exhibited errors in the IED and healthy durations of the same millisecond order of magnitude. For IED 3, the error is increased by a factor of 10, with a value of 0.30 seconds. However, also this value is small compared to the simulation duration.

An example of one of the four IEDs from Patient A with the corresponding synthetic signal from the SBI-derived parameter configuration is illustrated in Figure 18. The top channel displays the z state vari-

Table 2: Results from feature fitting procedure with corresponding real feature values of Patient A for all IEDs, using a 5-second simulation for neural network training. For all IEDs, an assigned real IED count with a value of 1 per 5-second interval was used and replicated successfully by the SBI-estimated configurations.

	IED	Real	Simulated	Error
IED duration (s)	1	1.72	1.70	0.02
	2	3.80	3.81	0.01
	3	4.24	3.91	0.33
	4	1.75	1.72	0.03
Healthy duration (s)	1	3.17	3.18	0.01
	2	1.09	1.07	0.02
	3	0.64	0.94	0.30
	4	3.14	3.16	0.02
IED count	1	1	1	0
	2	1	1	0
	3	1	1	0
	4	1	1	0

able, highlighting the detected IED interval as the region with a positive derivative (green-marked area). The corresponding LFP signal of the same node is seen in the channel below the z variable, highlighting its change in higher amplitude spiky behaviour. In the six bottom channels, we see the real iEEG signal where the IED is centred in the interval. The duration of the real and synthetic IED interval is nearly identical, having a 2-millisecond difference.

For the 15-second based neural network (Table 3), features of IED 2 and 3 are accurately replicated, having millisecond-level duration errors and a replicated IED count of 1. However, no IED is detected for the shorter IEDs 1 and 4, indicating that during the whole simulation of the SBI-derived parameter configuration, the model remains in its healthy state.

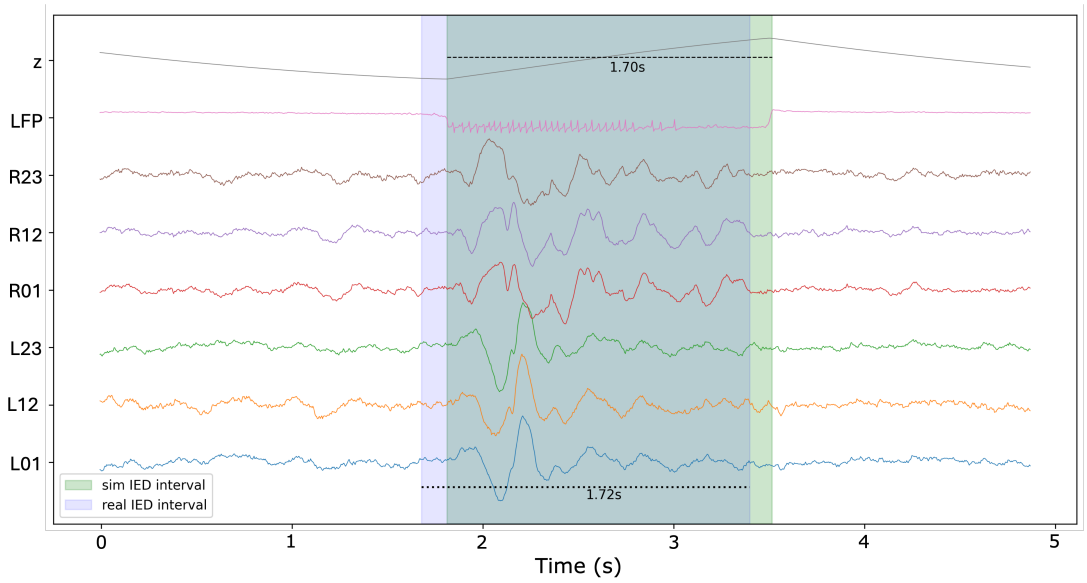

Figure 18: Real iEEG recording of an identified IED from Patient A, plotted in the bottom six channels (R23 up to L01). The blue marked period indicates the annotated IED interval. The upper two channels show both the z state variable and corresponding LFP (as defined by the Epileptor model) estimation of the epileptiform-generating node from SBI-identified parameters based on the real IED features.

Table 3: Results from feature fitting procedure with corresponding real feature values of Patient A for all IEDs, using a 15-second simulation for neural network training. For all IEDs, an assigned real IED count with a value of 1 per 15-second interval was used. The SBI-estimated configurations could not replicate this count for IED 1 and IED 4, resulting in a duration error equal to the IED duration itself.

	IED	Real	Simulated	Error
IED duration (s)	1	1.72	0	1.72
	2	3.80	3.80	0
	3	4.24	4.26	0.02
	4	1.75	0	1.75
Healthy duration (s)	1	13.18	14.90	1.72
	2	11.11	11.10	0.01
	3	10.66	10.64	0.02
	4	13.16	14.90	1.74
IED count	1	1	0	1
	2	1	1	0
	3	1	1	0
	4	1	0	1

The IED fitting results for Patient B, summarised in Figure 19, show the SBI-based synthetic IED durations plotted against their corresponding real durations. A first-order polynomial fit yields slope values of 0.84 (5-second network) and 0.90 (15-second network). It demonstrates accurate replication of real IED features within the tested duration range, which is particularly true for the first half of the duration range in both Figures a and b.

For the 5-second simulation-based neural network (Figure 19a), synthetic IED durations range from 0.79 to 4.07 seconds. The 15-second simulation-based neural network (Figure 19b) produces IED durations ranging from 2.12 to 12.13 seconds. Beyond these ranges, the model fails to replicate signal features. This corresponds with a non-oscillating z state variable (example in Figure 13a), causing no IED to be detected. When simulating large IED durations relative to the total duration (i.e. durations larger than 4.07 and 12.13 seconds), it is difficult for the model to fit a very dominant part of the signal duration as IED behaviour since this comes with great precision. Regarding the minimally detected durations of 0.79 and 2.12 seconds, the z state variable appears to be limited in simulating a small IED duration in proportion to the total duration. This we can calculate as the ratio of the IED duration relative to the healthy duration. Calculating this IED-healthy ratio reveals minimal differences between the two networks in both minimum and maximum ratios (Table 4). Additional scatter plots showing all ratio attempts for IED-feature replication are provided in Appendix D.

Table 4: The minimal and maximal IED-healthy duration ratios given for both neural networks.

	5-second simulation-based neural network	15-second simulation-based neural network
Minimal ratio	0.195	0.199
Maximal ratio	4.775	4.371

For all three parameters within the 15-second simulation-based neural network, a pattern can be seen in their parameter value for generating a certain IED duration. However, their behaviour in this differs. Figure 20 shows the relationship between synthetic IED duration and parameter values. The range on the y-axis is based on the domains of the three parameters. For x_0, the value decreases initially for increasing synthetic IED duration, followed by a switch to start increasing around 4.5 seconds. For K_s, we first observe a linear increase which flattens out and becomes constant. Lastly, r remains nearly constant over the whole duration range, indicating a very small range relative to the total domain of r results in the desired feature values.

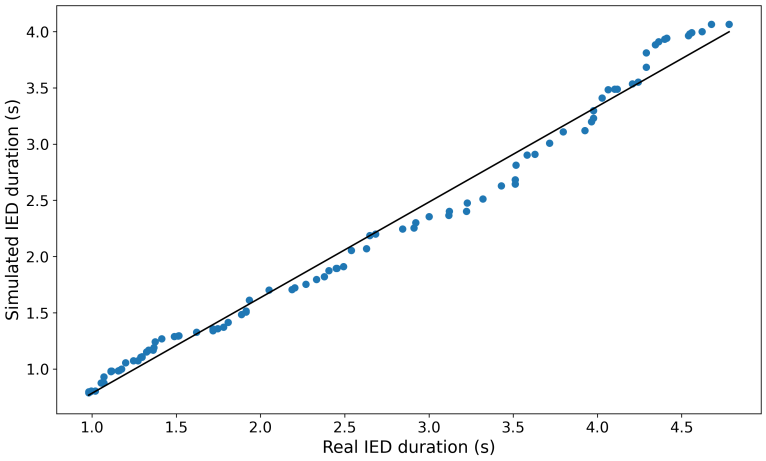

(a)

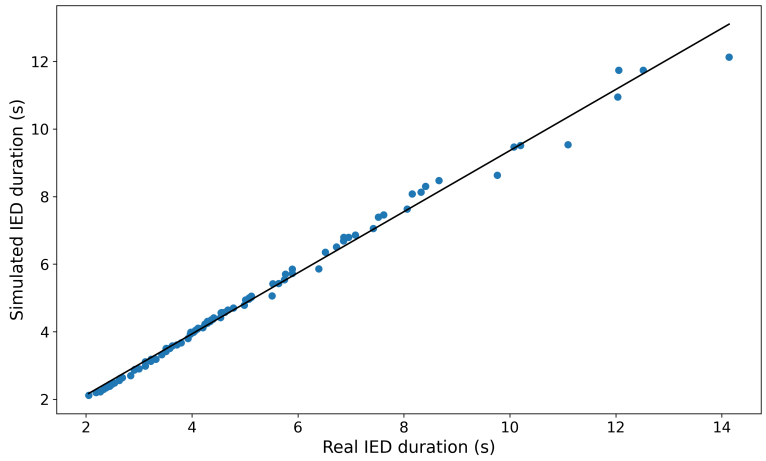

(b)

Figure 19: The detected IED duration from the synthetic signal of the SBI-estimated configuration, plotted against its corresponding real annotated IED duration feature found in Patient B. Figures a and b show the results of the neural network trained from 5-second and 15-second simulations, respectively. The black solid line represents the first-order polynomial fit of the data with values of 0.84 (5-second network) and 0.90 (15-second network).

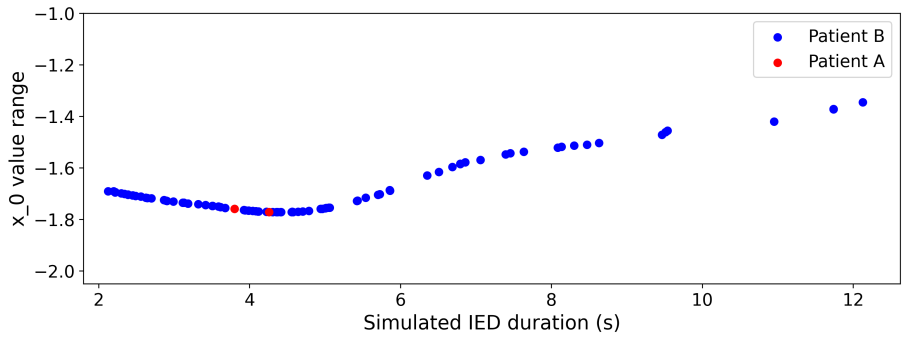

(a)

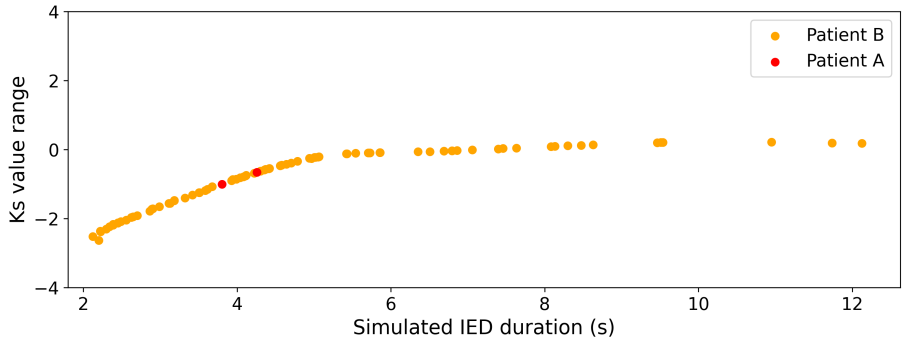

(b)

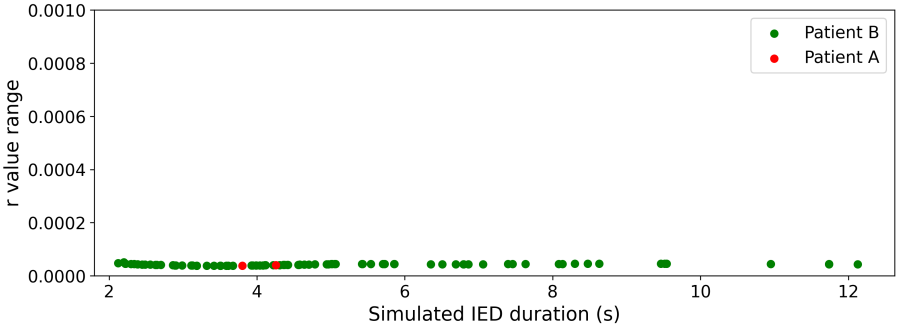

(c)

Figure 20: Parameter values for increasing simulated IED duration, using configurations of the data-fitted features derived from the 15-second simulation trained neural network from both Patient A and Patient B. (a) The initial value of x_0 decreases as the synthetic IED duration increases, before reversing and starting to increase around 4.5 seconds. (b) K_s shows initially a linear increase that gradually levels off and becomes constant. (c) r remains nearly constant across the entire duration range.

5 Discussion

In this study, we aimed to develop a personalised whole-brain model generating epileptiform activity in TVB, incorporating electrophysiological data for subsequent data-fitting methods. The model combined structural connectivity (from the TVB demonstration dataset) and mesoscopic Epileptor models to simulate macroscopic signals comparable to empirical data. SBI was employed for data fitting through neural network training to enable patient-specific simulations. Three separate analyses were conducted by training two neural networks, assigning parameter variation (of x_0, K_s and r) to one node in the model. The first synthetic analysis trained neural networks towards successful convergence to known parameter configurations that reproduced visually similar simulations, although a shift in the IED interval was observed. This same neural network was used to infer the parameters for real measured data, showing the SBI-estimated parameter configurations did not replicate any of the real iEEG patterns, related to healthy or IED morphology. The third analysis reduced high-dimensional data towards 3-dimensional features (IED duration, IED count and healthy duration), training a 5-second and 15-second simulation-based neural network. These features were replicated successfully by SBI-estimated configurations, although both durations required being in a specific range, relative to the total duration. We determined a minimal value of the IED-to-healthy duration ratio of 0.195 and 0.199 for the 5-second and 15-second simulation-based neural network respectively. Overall, these findings demonstrate the ability to combine TVB and SBI using real epileptiform data, although challenges were faced in capturing empirical iEEG characteristics using the Epileptor model.

The success of the synthetic data fitting demonstrated that SBI is capable of converging towards known parameter configurations. This supports its robustness in well-constrained scenarios. However, as we observed in Figure 14 for x_0 in particular, the probability distribution changes its shape with an increasing number of simulations and does not follow the expected pattern, from a broad to a narrow distribution. Possibly, this can be explained by the role of x_0 in the Epileptor dynamics, particularly when varying K_s and r parameters simultaneously. Mathematical analysis of the Epileptor showed x_0 plays a critical role in defining the system's equilibrium points, determining whether the model exhibits normal activity, a non-oscillatory state, or transitions between interictal and ictal states [46]. This suggests that near the healthy-to-epileptiform transition, small changes in x_0 can profoundly affect the system dynamics, resulting in bifurcations. However, as we are varying x_0 in its zone capable of generating epileptiform activity only, the model's dynamics in this range are less dependent on fine-tuning of x_0. As long as the bifurcation to the ictal state is enabled for all possible simulations, compensation by other parameters (i.e. r and K_s) allows a wider range of x_0 values to fit observed data, resulting in a broad posterior distribution compared to x_0 variation alone.

Analysing the results in Figure 15, we visualised the differences between the maximal posterior estimations of SBI and the reference values for all three parameters. First, the difference for x_0 and K_s temporarily increases compared to the starting number of 750 simulations. This decreases again for all three parameters, where we observed a stabilisation around 16,000 simulations, with the difference varying relatively constantly. This variation in the difference between the SBI-estimated and reference configuration is higher than anticipated. We also observe that the magnitude of variation from approximately 16,000 simulations, is similar between the parameters, relative to their domain. Plotting the synthetic data corresponding to fewer simulations could help determine whether signal overlap (and therefore convergence to the observed synthetic data) happened earlier in the process. If this is the case, we could conclude the parameter configuration leading to this particular simulation is not a high-sensitive configuration, but has multiple solutions, as long as the values remain within their domain.

The inability of SBI to replicate realistic EEG and IED patterns for real raw time series fitting, suggests that the model is limited in capturing the full complexity of patient-specific data. This limitation likely stems from using the Epileptor as a phenomenological model [34]. It aims to understand seizure dynamics using bifurcation theory. It was not designed for replicating (i)EEG signals containing IED-like features such as a transient followed by a slow after-wave according to standards from e.g. Mercier *et al.* [20]. In clinical applications, it has primarily been tested for its predictive power of the spatial organisation of the epileptiform-initiation and propagation zone before surgery [47]. This approach aims to correlate brain-based simulations with surgical outcomes, rather than capturing specific IED morphologies. In another study, SBI was already used for the TVB-Epileptor model to efficiently estimate the posterior distribution of parameters from sparse iEEG recordings [48]. Here, the focus was similar

compared to the previous research. It was demonstrated that SBI allows reliable inference of the critical epileptiform-generating variable x_0 on a spatial scale compared to estimations made by clinical expertise. Both studies highlight the Epileptor's capability to generate system bifurcations that accurately reflect seizure onset, propagation, and termination. However, unlike these studies, our objective was not spatial mapping of epileptiform activity but rather the reproduction of patient-specific IED patterns. Given the uncertainties in whether the TVB-Epileptor can generate such patterns, the failure of SBI to fit real EEG data may indicate model misspecification.

SBI misspecification arises when the real data distribution falls outside the range of distributions the model can generate [49]. That is, if the true data-generating process $p^*(x_0)$ does not exist in the set of distributions defined by the model $P(x_0 \mid \theta)$, no parameter configuration can be found that matches the simulated and real iEEG signals. The likelihood that SBI itself causes fitting deficiencies is expected to be lower, based on the results of the synthetic data fitting and existing SBI networks that have performed adequately in the literature [41]. SBI has been shown to operate effectively in parameter estimation of high-dimensional (image or time-series) data, even when confronted with the additional challenge of having multiple data dimensions that are uninformative about the true parameter configuration. Therefore, constraints in the Epileptor model in capturing detailed IED characteristics may be the dominant limiting factor.

To address these constraints, we adapted the approach from fitting the morphology of raw time series to a feature-based fitting strategy. We focused on extracting specific low-dimensional features (IED duration, IED count and healthy duration) from simulated and empirical time series. Therefore, we rephrased our aim to prioritize capturing the key dynamical properties related to IED behaviour. We thus can take advantage of the Epileptor's design as a bifurcation-driven model, excelling at state transitions between healthy and unhealthy activity. Another advantage we gained from this strategy was the reduction of neural network complexity, facilitating training and convergence.

The success of the feature-fitting approach could be observed in the SBI-estimated parameter configurations, which replicated adequate IED and healthy durations under specific conditions. Compared to the real durations, we observed only millisecond-order differences in most SBI-estimated IED durations in both patients. However, constraints emerged when simulating extreme cases, such as very short IED durations. The minimal IED-to-healthy duration ratios observed in our models (0.195 for the 5-second network and 0.199 for the 15-second network) suggest a limitation in the Epileptor's flexibility. These constraints likely stem from the z-variable, which governs the system's slows dynamics and imposes fixed limits on the timing of transitions between different states. Furthermore, we again face the problem of the phenomenological state of the model. The biophysical explanation of why the system enters this pathological IED state is lacking, which makes it difficult to interpret the underlying causes. This absence of insights could also hinder the longer-term goal, such as understanding the physiological basis for the distinction between effective and non-effective DBS treatment.

The Epileptor is one example of a mesoscale model in epilepsy. However, various other models have been introduced, including those focusing on IED-like behaviour. Suggestions interesting for this project are models capable of both IED-like and seizure-like events, where the influence of DBS parameter variation on the likelihood of seizure generation can be investigated. If we can link these influences to the model's intrinsic properties, they may provide a deeper understanding of the biophysical mechanisms underlying seizure likelihood reduction.

For instance, a study conducted by Wang *et al.* used a Jansen's neural mass model (JNMM) to determine control parameters of a DBS-strategy based on a proportional-integral (PI) controller for suppressing epileptic activity [50]. The JNMM is based on the imbalance between excitation and inhibition which results from hyper-excitation or low inhibition. The design objective was to determine the PI controller parameter values that stabilised the unstable JNMM caused by abnormal parameter values such that homeostasis of the JNMM was maintained and the high-amplitude epileptic activity was suppressed. Wendling *et al.* proposed a hippocampal network model, incorporating high-frequency (gamma band) oscillations and inhibitory/excitatory interactions [51]. This model extended previous approaches in inhibitory/excitatory imbalance by accounting for i) distinct inhibitory mechanisms of different interneuron types on pyramidal cells and ii) functional reorganisation of inhibition in epileptic tissue. Both interictal periods (with normal background activity and sporadic spikes) and ictal activities (involving

sustained spike activity and slow rhythmic) closely resemble empirical data. Both examples differ from the Epileptor as they incorporate physiological mechanisms describing excitation/inhibition balance. Potentially this could enhance the understanding of seizure and IED generation in (i)EEG signals while generating EEG morphology that more closely resembles what we observed in real data. When combined with in-silico DBS treatment, effective and ineffective seizure reduction effects may be realised for further examination.

Therefore, another suggestion could be to utilize a model which directly determines the influence of treatment in drug-resistant epilepsy on the likelihood of seizure generation in a variable. Sinha *et al.*, defined the likelihood variable as the inverse of the average transition time from healthy to seizure state for nodes in a given network. Therefore nodes with a short transition time were defined as highly active in generating epileptiform activity [52]. Involving the likelihood variable first in the personalised model development during parameter estimation and later in DBS influence prediction would allow a more direct evaluation of the model's ability to replicate regions with a high and low risk for seizure generation.

5.1 Limitations and future work

This study also faced several limitations and methodological simplifications that may have influenced findings and generalizability. Starting with model-related simplifications, an important example is the absence of personalised structural connectivity elements in the model. This is, especially in the TVB, seen as a key feature towards personalised whole-brain modelling for detecting differences in a pathological and healthy state. Much of the complexity of brain signals such as EEG arises from the coordination of the interconnected neural masses rather than the intrinsic dynamics on the microscopic unit of the large-scale network, (i.e. the neural mass) [53]. In epilepsy, particularly in temporal lobe epilepsy (TLE), patients show several alterations in structural connectivity measures. This involves e.g. a decreased fibre density in the limbic subnetwork and decreased global network efficiency [54], [55]. However, it is not yet understood how these changes relate to the epileptic condition and how they give rise to changes (if any) in functional connectivity, i.e. the variables in modelling [56]. Nevertheless, the lack of patient-specific structural connectivity likely limits the accuracy of synthetic signal propagation, especially in pathological states. Incorporating this in future work will enhance the biological realism of the model. Additionally, further (literature) research into the impact of personalised structural connectivity in epilepsy modelling could help clarify its added value and improve the robustness of patient-specific simulations.

We chose to simplify the TVB-Epileptor model by enabling only one node to generate epileptiform activity. This constrained the ability to spread the IED behaviour throughout the brain. In real-world scenarios, this spreading leads to variability in IED duration and morphology across different brain areas. Also in the VEP as proposed by Jirsa *et al.*, differences were observed between seizure duration and timing of initiation and termination seizure patterns between EEG channels. In this study, multiple nodes were enabled to generate seizure activity and additional nodes were assigned to propagate the activity using the x_0 variable. The synthetic IED durations in this study were deviating from empirical observations and the VEP by remaining uniform across all regions. Moreover, the decision on what node was chosen to be epileptiform-active did not support patient-specific knowledge. A potential solution to characterize the correct number and the correct locations of epileptiform-initiating and/or propagating nodes would involve techniques such as source reconstruction. It allows reconstruction of the responsible sources for the measured signal on a macroscopic scale (scalp or intracranial EEG) [57]. This potentially enables the identification of key epileptiform-initiating and propagating regions and would therefore improve parameter optimisation methods. Furthermore, identifying multiple regions related to epileptiform-initiation activity may enable us to improve the variability in IED duration and morphology.

Subsequently, the number of varied parameters for SBI data-fitting purposes within the node was restricted to three, whereas a total of 10 parameters are used to describe the Epileptor's behaviour (Table 1). This limitation likely restricted the exploration of the full dynamic range of the Epileptor model. For example, parameters such as τ_0 and τ_2, which govern time scales, or coupling terms between fast and slow ensembles, could significantly influence the dynamics of IED initiation and termination. Future studies should consider expanding the parameter space to capture a broader spectrum of behaviours of the Epileptor. This may require additional computational efficiency through parallelisation modelling techniques.

While the final SBI analysis involving data-reduction using 3-dimensional features improves model fit, our feature-detection approach diverges from standard dimensionality-reduction techniques. For example, those used in ABC inference often aim to derive features capturing the maximum information about the parameters across the entire dataset [58]. Another automated approach was proposed by Huang *et al.*, who tackled the challenges of both SBI misspecification and data reduction directly [59]. Here, a regularised loss function was introduced that remained informative about the parameters while penalizing statistics that increase the mismatch between data and the model. With empirical data, the method showed robust inference in misspecified scenarios. Future work may thus explore more on learning methods of robust data-reduction for SBI under model misspecification. If this work is performed with the Epileptor, it could help in quantifying more systematically what information of the TVB-Epileptor model is most important to capture, with respect to the real data.

Besides the developed TVB-Epileptor model, methodological limitations in SBI were noted. The quality of the obtained posteriors was only partially evaluated, as synthetic data fitting involved testing a single parameter configuration. This leaves open questions about the robustness of the neural network across a broader parameter space, as the posteriors should always be checked carefully before relying on it in downstream tasks [42]. To extend this an additional method can be applied where we sample more parameter configurations from the prior (randomised parameter values picked from their corresponding domain) and obtain the SBI-estimated parameter configurations. Comparing this multiple times for known parameter configurations allows a more solid statement on whether or not poor-quality approximations of the neural network are avoided.

Finally, a high rate of invalid simulations is observed, particularly during feature fitting. This may be solved with adaptive sampling strategies, involving additional preparation steps before simulating the prior-sampled parameter configurations. An example is using truncated proposals, i.e. rewritten prior parameter ranges to sample from for simulation [60]. The method first samples from the original prior and runs the simulator. Then a neural network is trained to approximate the posterior. In subsequent rounds, parameters are sampled from the prior but rejected if they lie outside the support of the approximate posterior. These improved parameter ranges can reduce computational inefficiencies as they can be trained with maximum likelihood. However, we must keep in mind validation behind of additional components are important. Regarding the additional data-reduction step towards feature fitting, the algorithm was built such that simulations leading to non-observed IEDs (i.e. due to a non-oscillatory z state variable), were counted as invalid as well. This probably will have increased the number of invalid simulations a lot.

6 Conclusion

This thesis explored i) the development of a personalised computational macro-scale brain model capable of simulating (features of) epileptiform activity and ii) the integration of empirical optimisation techniques using iEEG data. The TVB platform served as a foundation for the construction of the whole-brain model. We connected dynamical models on the mesoscale level (nodes), allowing the potential inclusion of personalised connectivity metrics based on structural and functional MRI data. However, this study did not achieve the integration of personalised connectivity matrices. We used the Epileptor to define node activity, with the left hippocampus having the ability to generate epileptiform activity.

To optimize model parameters based on real patient data, we employed SBI, a neural network-driven parameter estimation approach. Synthetic data fitting analysis concluded that SBI can identify parameter configurations close to the reference parameter values, obtaining visually similar simulations. However, when applying SBI to real iEEG time series the optimisation failed to converge towards parameter configurations capable of reproducing IED morphology as seen in clinical recordings. This outcome suggests model misspecification, where the real data distribution falls outside the range of distributions the TVB-Epileptor model can generate. To address these model constraints, we shifted from fitting IED morphology towards low-dimensional features (IED duration, IED count, healthy duration). SBI was able to converge towards parameter configurations successfully, producing simulations with millisecond-order errors. Despite this, limitations persisted, particularly in simulating short IED durations relative to long healthy intervals. This likely reflects the limitations of the Epileptor's z-variable which governs slow dynamics and imposes fixed limits on state transitions. Furthermore, the Epileptor lacks a biophysical basis for explaining why the system transitions into an IED state, limiting its ability to capture the intrinsic mechanisms underlying epileptiform activity.

Overall, these findings highlight the ability of using SBI in parameter optimisation methods, combined with the TVB platform. However, the SBI analyses with real data underscore more exploration and examination are necessary, resulting in improved methodologies to capture broader EEG characteristics. The Epileptor model has shown in literature the capability of generating system bifurcations that accurately reflect seizure onset, propagation, and termination. However, uncertainties still exist in capturing IED features related to morphology and extreme cases in IED duration. A deeper exploration of the Epileptor's limitations could gain better insights into using the model as a prediction tool for seizure likelihood reduction due to DBS. Besides this, integrating different or complementary modelling frameworks should be investigated to improve the biological realism, flexibility, and accuracy of the personalised TVB-Epileptor model. Lastly, future work should aim to integrate patient-specific connectivity and expand the explored parameter range for data-fitting purposes.

References

[1] E. Beghi, "The Epidemiology of Epilepsy", *Neuroepidemiology*, vol. 54, no. 2, pp. 185–191, 2020, ISSN: 14230208. DOI: 10.1159/000503831.

[2] S. Weinstein, "Seizures and epilepsy: An overview", *Epilepsy: The Intersection of Neurosciences, Biology, Mathematics, Engineering, and Physics*, pp. 65–77, 2016. DOI: 10.1201/b10866-10.

[3] L. Dalic and M. J. Cook, "Managing drug-resistant epilepsy: Challenges and solutions", *Neuropsychiatric Disease and Treatment*, vol. 12, pp. 2605–2616, Oct. 2016, ISSN: 11782021. DOI: 10.2147/NDT.S84852.

[4] D. C. Klooster, A. J. de Louw, A. P. Aldenkamp, *et al.*, "Technical aspects of neurostimulation: Focus on equipment, electric field modeling, and stimulation protocols", *Neuroscience & Biobehavioral Reviews*, vol. 65, pp. 113–141, Jun. 2016, ISSN: 0149-7634. DOI: 10.1016/J.NEUBIOREV.2016.02.016.

[5] V. Salanova, "Deep brain stimulation for epilepsy", *Epilepsy & Behavior*, vol. 88, pp. 21–24, Nov. 2018, ISSN: 1525-5050. DOI: 10.1016/J.YEBEH.2018.06.041.

[6] M. C. H. Li, —. Mark, and J. Cook, "Deep brain stimulation for drug-resistant epilepsy", 2017. DOI: 10.1111/epi.13964. [Online]. Available: https://onlinelibrary.wiley.com/doi/10.1111/epi.13964.

[7] J. M. Meier, D. Perdikis, A. Blickensdörfer, *et al.*, "Virtual deep brain stimulation: Multiscale co-simulation of a spiking basal ganglia model and a whole-brain mean-field model with The Virtual Brain", *Experimental Neurology*, vol. 354, no. May, 2022, ISSN: 10902430. DOI: 10.1016/j.expneurol.2022.114111.

[8] D. Depannemaecker, A. Ezzati, H. E. Wang, V. Jirsa, and C. Bernard, "From phenomenological to biophysical models of seizures", *Neurobiology of Disease*, vol. 182, no. February, p. 106 131, 2023, ISSN: 1095953X. DOI: 10.1016/j.nbd.2023.106131. [Online]. Available: https://doi.org/10.1016/j.nbd.2023.106131.

[9] V. K. Jirsa, T. Proix, D. Perdikis, *et al.*, "The Virtual Epileptic Patient: Individualized whole-brain models of epilepsy spread", 2016. DOI: 10.1016/j.neuroimage.2016.04.049. [Online]. Available: http://dx.doi.org/10.1016/j.neuroimage.2016.04.049.

[10] S. Abramovici and A. Bagić, "Epidemiology of epilepsy", in *Handbook of Clinical Neurology*, 1st ed., vol. 138, Elsevier B.V., 2016, pp. 159–171, ISBN: 9780128029732. DOI: 10.1016/B978-0-12-802973-2.00010-0. [Online]. Available: http://dx.doi.org/10.1016/B978-0-12-802973-2.00010-0.

[11] P. Chauhan, S. E. Philip, G. Chauhan, and S. Mehra, "The Anatomical Basis of Seizures", *Epilepsy*, pp. 15–24, Apr. 2022. DOI: 10.36255/EXON-PUBLICATIONS-EPILEPSY-ANATOMICAL-BASIS. [Online]. Available: https://www.ncbi.nlm.nih.gov/books/NBK580614/.

[12] M. van Putten, *Dynamics of neural networks*. 2013, pp. 489–512, ISBN: 9781439853313. DOI: 10.1201/b14756.

[13] P. Kwan, S. C. Schachter, and M. J. Brodie, "Drug-Resistant Epilepsy", pp. 919–926, 2011.

[14] S. Miocinovic, S. Somayajula, S. Chitnis, and J. L. Vitek, "History, Applications, and Mechanisms of Deep Brain Stimulation", *JAMA Neurology*, vol. 70, no. 2, pp. 163–171, Feb. 2013, ISSN: 2168-6149. DOI: 10.1001/2013.JAMANEUROL.45. [Online]. Available: https://jamanetwork.com/journals/jamaneurology/fullarticle/1391074.

[15] S. J. Smith, "EEG in the diagnosis, classification, and management of patients with epilepsy", *Journal of Neurology, Neurosurgery & Psychiatry*, vol. 76, no. suppl 2, pp. ii2–ii7, Jun. 2005, ISSN: 0022-3050. DOI: 10.1136/JNNP.2005.069245. [Online]. Available: https://jnnp.bmj.com/content/76/suppl_2/ii2%20https://jnnp.bmj.com/content/76/suppl_2/ii2.abstract.

[16] E. H. Smith, J. Y. Liou, E. M. Merricks, *et al.*, "Title: Human interictal epileptiform discharges are bidirectional traveling waves echoing ictal discharges", *eLife*, vol. 11, Jan. 2022, ISSN: 2050084X. DOI: 10.7554/ELIFE.73541.

[17] E. C. Conrad, S. B. Tomlinson, J. N. Wong, *et al.*, "Spatial distribution of interictal spikes fluctuates over time and localizes seizure onset", *Brain*, vol. 143, no. 2, pp. 554–569, Feb. 2020, ISSN: 0006-8950. DOI: 10.1093/BRAIN/AWZ386. [Online]. Available: https://dx.doi.org/10.1093/brain/awz386.

[18] M. O. Baud, J. K. Kleen, E. A. Mirro, *et al.*, "Multi-day rhythms modulate seizure risk in epilepsy", *Nature Communications*, vol. 9, no. 1, pp. 1–10, 2018, ISSN: 20411723. DOI: 10.1038/s41467-017-02577-y. [Online]. Available: http://dx.doi.org/10.1038/s41467-017-02577-y.

[19] M. A. Kural, L. Duez, V. Sejer Hansen, *et al.*, "Criteria for defining interictal epileptiform discharges in EEG: A clinical validation study", *Neurology*, vol. 94, no. 20, E2139–E2147, 2020, ISSN: 1526632X. DOI: 10.1212/WNL.0000000000009439.

[20] M. R. Mercier, A. S. Dubarry, F. Tadel, *et al.*, "Advances in human intracranial electroencephalography research, guidelines and good practices", *NeuroImage*, vol. 260, no. June, p. 119 438, 2022, ISSN: 10959572. DOI: 10.1016/j.neuroimage.2022.119438. [Online]. Available: https://doi.org/10.1016/j.neuroimage.2022.119438.

[21] R. A. Stefanescu, R. G. Shivakeshavan, and S. S. Talathi, "Computational models of epilepsy", DOI: 10.1016/j.seizure.2012.08.012. [Online]. Available: http://dx.doi.org/10.1016/j.seizure.2012.08.012.

[22] O. Sporns, "Brain Connectivity", *Scholarpedia*, vol. 2, no. 10, p. 4695, 2007. DOI: 10.4249/scholarpedia.4695.

[23] E. D'Angelo and V. Jirsa, "The quest for multiscale brain modeling", *Trends in Neurosciences*, vol. 45, no. 10, pp. 777–790, Oct. 2022, ISSN: 0166-2236. DOI: 10.1016/J.TINS.2022.06.007.

[24] P. Sanz-Leon, S. A. Knock, A. Spiegler, and V. K. Jirsa, "Mathematical framework for large-scale brain network modeling in The Virtual Brain", *NeuroImage*, vol. 111, pp. 385–430, May 2015, ISSN: 1053-8119. DOI: 10.1016/J.NEUROIMAGE.2015.01.002.

[25] J. C. de Munck, B. W. van Dijk, and H. Spekreijse, "Mathematical Dipoles are Adequate to Describe Realistic Generators of Human Brain Activity", *IEEE Transactions on Biomedical Engineering*, vol. 35, no. 11, pp. 960–966, 1988, ISSN: 15582531. DOI: 10.1109/10.8677.

[26] J. Vorwerk, R. Oostenveld, M. C. Piastra, L. Magyari, and C. H. Wolters, "The FieldTrip-SimBio pipeline for EEG forward solutions", *BioMedical Engineering Online*, vol. 17, no. 1, Mar. 2018, ISSN: 1475925X. DOI: 10.1186/S12938-018-0463-Y. [Online]. Available: https://www.fieldtriptoolbox.org/workshop/ohbm2018/forward/.

[27] H. Hallez, B. Vanrumste, R. Grech, *et al.*, "Review on solving the forward problem in EEG source analysis", *Journal of NeuroEngineering and Rehabilitation*, vol. 4, no. 1, pp. 1–29, Nov. 2007, ISSN: 17430003. DOI: 10.1186/1743-0003-4-46/FIGURES/19. [Online]. Available: https://jneuroengrehab.biomedcentral.com/articles/10.1186/1743-0003-4-46.

[28] P. Sanzleon, S. A. Knock, M. M. Woodman, *et al.*, "The virtual brain: A simulator of primate brain network dynamics", *Frontiers in Neuroinformatics*, vol. 7, no. MAY, p. 47 900, Jun. 2013, ISSN: 16625196. DOI: 10.3389/FNINF.2013.00010/ABSTRACT. [Online]. Available: www.frontiersin.org.

[29] T. Proix, A. Spiegler, M. Schirner, S. Rothmeier, P. Ritter, and V. K. Jirsa, "How do parcellation size and short-range connectivity affect dynamics in large-scale brain network models?", *NeuroImage*, vol. 142, pp. 135–149, Nov. 2016, ISSN: 1095-9572. DOI: 10.1016/J.NEUROIMAGE.2016.06.016. [Online]. Available: https://pubmed.ncbi.nlm.nih.gov/27480624/.

[30] B. Fischl, "FreeSurfer", *NeuroImage*, vol. 62, no. 2, pp. 774–781, Aug. 2012, ISSN: 1053-8119. DOI: 10.1016/J.NEUROIMAGE.2012.01.021.

[31] M. Jenkinson, C. F. Beckmann, T. E. Behrens, M. W. Woolrich, and S. M. Smith, "FSL", *NeuroImage*, vol. 62, no. 2, pp. 782–790, Aug. 2012, ISSN: 1053-8119. DOI: 10.1016/J.NEUROIMAGE.2011.09.015. [Online]. Available: https://linkinghub.elsevier.com/retrieve/pii/S1053811911010603.

[32] S. Fuhrmann, J. Ackermann, T. Kalbe, and M. Goesele, "Direct Resampling for Isotropic Surface Remeshing", 2010. DOI: 10.2312/PE/VMV/VMV10/009-016.

[33] J. D. Tournier, F. Calamante, and A. Connelly, "MRtrix: Diffusion tractography in crossing fiber regions", *International Journal of Imaging Systems and Technology*, vol. 22, no. 1, pp. 53–66, 2012, ISSN: 08999457. DOI: 10.1002/ima.22005.

[34] V. K. Jirsa, W. C. Stacey, P. P. Quilichini, A. I. Ivanov, and C. Bernard, "On the nature of seizure dynamics", *Brain*, vol. 137, no. 8, pp. 2210–2230, 2014, ISSN: 14602156. DOI: 10.1093/brain/awu133.

[35] V. Jirsa, H. Wang, P. Triebkorn, *et al.*, "Personal View Personalised virtual brain models in epilepsy", vol. 22, p. 443, 2023. DOI: 10.1016/S1474-4422(23)00008-X. [Online]. Available: https://www.thevirtualbrain..

[36] T. Proix, F. Bartolomei, M. Guye, and V. K. Jirsa, "Individual brain structure and modelling predict seizure propagation", *Brain*, vol. 140, no. 3, pp. 641–654, 2017, ISSN: 14602156. DOI: 10.1093/brain/awx004.

[37] Q. Wang, G. Jin, T. Yu, F. Bartolomei, and L. Ren, "Emerging personalized virtual brain models: next-generation resection neurosurgery for drug-resistant epilepsy?", *Acta Epileptologica*, vol. 5, no. 1, pp. 1–4, 2023, ISSN: 25244434. DOI: 10.1186/s42494-023-00128-1. [Online]. Available: https://doi.org/10.1186/s42494-023-00128-1.

[38] T. Proix, F. Bartolomei, P. Chauvel, C. Bernard, and V. K. Jirsa, "Permittivity Coupling across Brain Regions Determines Seizure Recruitment in Partial Epilepsy", *Journal of Neuroscience*, vol. 34, no. 45, pp. 15 009–15 021, Nov. 2014, ISSN: 0270-6474. DOI: 10.1523/JNEUROSCI.1570-14.2014. [Online]. Available: https://www.jneurosci.org/content/34/45/15009%20https://www.jneurosci.org/content/34/45/15009.abstract.

[39] V. Jirsa, H. Wang, P. Triebkorn, *et al.*, "Personalised virtual brain models in epilepsy", *The Lancet Neurology*, vol. 22, no. 5, pp. 443–454, May 2023, ISSN: 1474-4422. DOI: 10.1016/S1474-4422(23)00008-X.

[40] K. Cranmer, J. Brehmer, and G. Louppe, "The frontier of simulation-based inference", *Proceedings of the National Academy of Sciences of the United States of America*, vol. 117, no. 48, pp. 30 055–30 062, Dec. 2020, ISSN: 10916490. DOI: 10.1073/PNAS.1912789117/ASSET/909FB0B7-567B-40FB-9B24-33893A76BD05/ASSETS/IMAGES/LARGE/PNAS.1912789117FIG01.JPG. [Online]. Available: https://www.pnas.org/doi/abs/10.1073/pnas.1912789117.

[41] D. S. Greenberg, M. Nonnenmacher, and J. H. Macke, "Automatic Posterior Transformation for Likelihood-free Inference", 2019.

[42] A. Delaunoy, "Towards Reliable Simulation-based Inference", 2024.

[43] G. Papamakarios and I. Murray, "Fast ϵ-free Inference of Simulation Models with Bayesian Conditional Density Estimation", *Advances in Neural Information Processing Systems*, pp. 1036–1044, May 2016, ISSN: 10495258. [Online]. Available: https://arxiv.org/abs/1605.06376v4.

[44] P. J. Gonçalves, J. M. Lueckmann, M. Deistler, *et al.*, "Training deep neural density estimators to identify mechanistic models of neural dynamics", *eLife*, vol. 9, pp. 1–46, Sep. 2020, ISSN: 2050084X. DOI: 10.7554/ELIFE.56261.

[45] A. Tejero-Cantero, J. Boelts, M. Deistler, *et al.*, "sbi: A toolkit for simulation-based inference", DOI: 10.21105/joss.02505. [Online]. Available: https://github.com/conormdurkan/lfi;.

[46] K. E. Houssaini, C. Bernard, and V. K. Jirsa, "The epileptor model: A systematic mathematical analysis linked to the dynamics of seizures, refractory status epilepticus, and depolarization block", *eNeuro*, vol. 7, no. 2, 2020, ISSN: 23732822. DOI: 10.1523/ENEURO.0485-18.2019.

[47] T. E. Proix, F. Bartolomei, M. Guye, and V. K. Jirsa, "Individual brain structure and modelling predict seizure propagation", DOI: 10.1093/awx018.

[48] M. Hashemi, A. N. Vattikonda, J. Jha, *et al.*, "Amortized Bayesian inference on generative dynamical network models of epilepsy using deep neural density estimators", *Neural Networks*, vol. 163, pp. 178–194, Jun. 2023, ISSN: 0893-6080. DOI: 10.1016/J.NEUNET.2023.03.040.

[49] A. Wehenkel, J. L. Gamella, O. S. Apple, *et al.*, "Addressing Misspecification in Simulation-based Inference through Data-driven Calibration",

[50] J. Wang, E. Niebur, J. Hu, and X. Li, "Suppressing epileptic activity in a neural mass model using a closed-loop proportional-integral controller", *Scientific Reports 2016 6:1*, vol. 6, no. 1, pp. 1–12, Jun. 2016, ISSN: 2045-2322. DOI: 10.1038/srep27344. [Online]. Available: https://www.nature.com/articles/srep27344.

[51] F. Wendling, F. Bartolomei, J. J. Bellanger, and P. Chauvel, "Epileptic fast activity can be explained by a model of impaired GABAergic dendritic inhibition", DOI: 10.1046/j.1460-9568.2002.01985.x. [Online]. Available: https://onlinelibrary.wiley.com/doi/10.1046/j.1460-9568.2002.01985.x.

[52] N. Sinha, J. Dauwels, M. Kaiser, *et al.*, "Predicting neurosurgical outcomes in focal epilepsy patients using computational modelling", *Brain*, vol. 140, no. 2, pp. 319–332, Feb. 2017, ISSN: 0006-8950. DOI: 10.1093/BRAIN/AWW299. [Online]. Available: https://dx.doi.org/10.1093/brain/aww299.

[53] V. Jirsa, *UNDERSTANDING COMPLEX SYSTEMS Handbook on Brain Connectivity*, A. McIntosh, Ed. Springer Complexity, 2007, p. 525, ISBN: 978-3-540-71462-0.

[54] L. Bonilha, T. Nesland, G. U. Martz, *et al.*, "Medial temporal lobe epilepsy is associated with neuronal fibre loss and paradoxical increase in structural connectivity of limbic structures", *Journal of Neurology, Neurosurgery & Psychiatry*, vol. 83, no. 9, pp. 903–909, Sep. 2012, ISSN: 0022-3050. DOI: 10.1136/JNNP-2012-302476. [Online]. Available: https://jnnp.bmj.com/content/83/9/903%20https://jnnp.bmj.com/content/83/9/903.abstract.

[55] M. N. DeSalvo, L. Douw, N. Tanaka, C. Reinsberger, and S. M. Stufflebeam, "Altered structural connectome in temporal lobe epilepsy", *Radiology*, vol. 270, no. 3, pp. 842–848, Nov. 2014, ISSN: 15271315. DOI: 10.1148/RADIOL.13131044/SUPPL{_}FILE/RADIOL.13131044.SUPPL. [Online]. Available: https://pubs.rsna.org/doi/10.1148/radiol.13131044.

[56] P. N. Taylor, Y. Wang, G. Marc, *et al.*, "A computational study of stimulus driven epileptic seizure abatement", *PLoS ONE*, vol. 9, no. 12, pp. 1–27, 2014, ISSN: 19326203. DOI: 10.1371/journal.pone.0114316.

[57] C. M. Michel and D. Brunet, "EEG source imaging: A practical review of the analysis steps", *Frontiers in Neurology*, vol. 10, no. APR, p. 446 653, Apr. 2019, ISSN: 16642295. DOI: 10.3389/FNEUR.2019.00325/BIBTEX. [Online]. Available: http://www.uzh.ch/keyinst/loreta.htm.

[58] M. G. Blum, M. A. Nunes, D. Prangle, and S. A. Sisson, "A comparative review of dimension reduction methods in approximate bayesian computation", *Statistical Science*, vol. 28, no. 2, pp. 189–208, 2013, ISSN: 08834237. DOI: 10.1214/12-STS406.

[59] D. Huang, A. Bharti, A. H. Souza, L. Acerbi, and S. Kaski, "Learning Robust Statistics for Simulation-based Inference under Model Misspecification",

[60] M. Deistler, P. J. Gonçalves, and J. H. Macke, "Truncated proposals for scalable and hassle-free simulation-based inference", *Advances in Neural Information Processing Systems*, vol. 35, Oct. 2022, ISSN: 10495258. [Online]. Available: https://arxiv.org/abs/2210.04815v2.

Appendices

A AI statement

During the preparation of this work, the author used ChatGPT in order to i) improve the correctness and clarity in the writing style and ii) assist in coding debugging issues, and Grammarly, in order to i) detect misspellings and ii) check proposed grammar-related improvements. After using these tools, the author reviewed and edited the content as needed and takes full responsibility for the content of the work.

B Feature detection - correct scenarios

In Figures 21 and 22, four different examples of feature detection scenarios are given. In all figures, the IED duration is illustrated as the dashed blue line, with the corresponding time given in seconds. The detected initiation and termination are marked by the green and red dots, respectively. The red solid line indicates the identified healthy duration. This also represents the broader variability of scenarios that were observed. In Figure 21, different IED lengths are illustrated, with relatively short and long IED durations in Figure 21a and Figure 22b, respectively. In Figure 22a, we observe the detection of multiple shot IEDs, with short intermediate healthy intervals as depicted in blue.

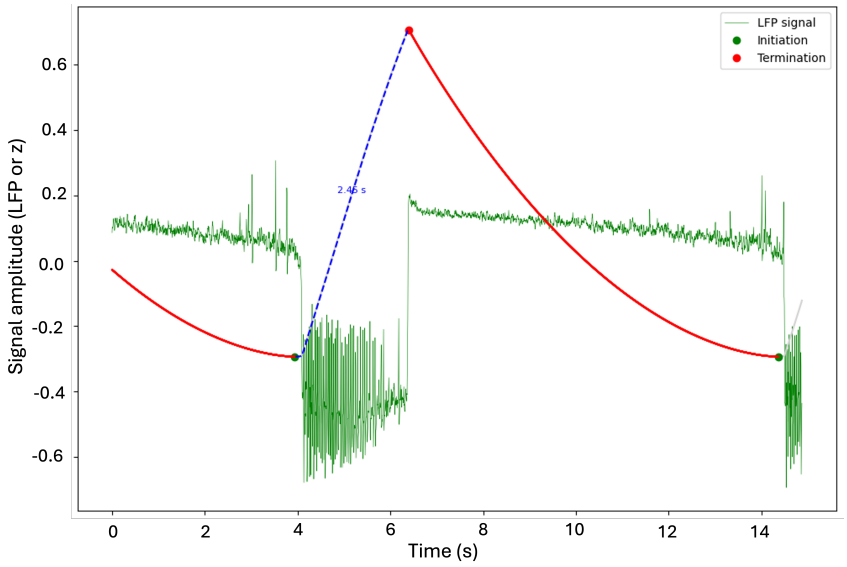

(a)

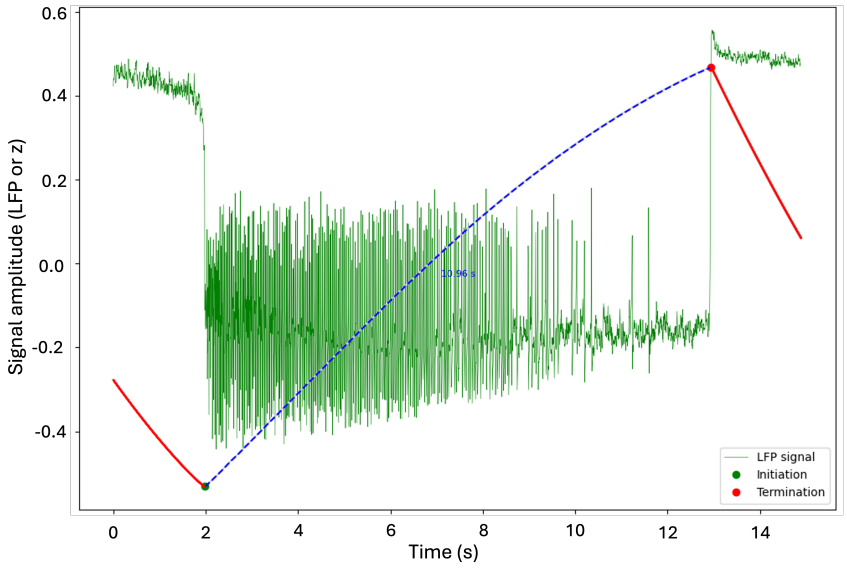

(b)

Figure 21: The first two out of three examples of correct feature detection in a 15-second interval. The IED duration is illustrated as the dashed blue line, with the corresponding time given in seconds. The detected initiation and termination are marked by the green and red dots, respectively. The red solid line indicates the identified healthy duration. (a) A short IED with 2.46 seconds duration. (b) A long IED with 10.96 seconds duration.

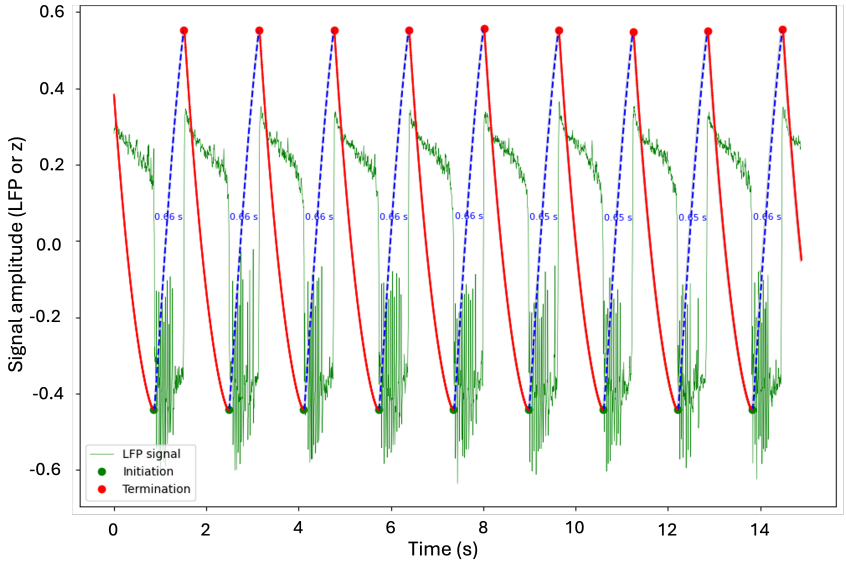

Figure 22: The third example of correct feature detection in a 15-second interval. The IED duration is illustrated as the dashed blue line, with the corresponding time given in seconds. The detected initiation and termination are marked by the green and red dots, respectively. The red solid line indicates the identified healthy duration. In total, 9 short IEDs occur, which are interrupted by short healthy intervals.

C Real data fitting, additional IEDs

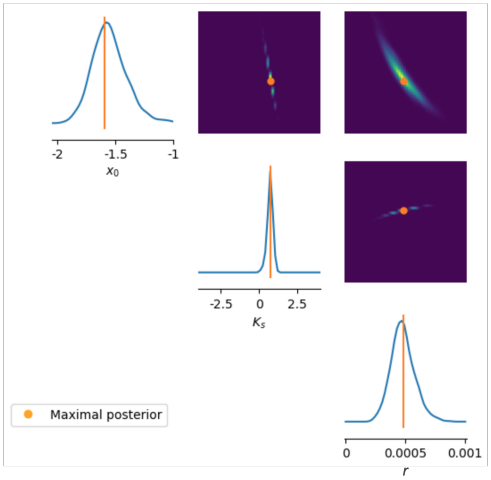

(a)

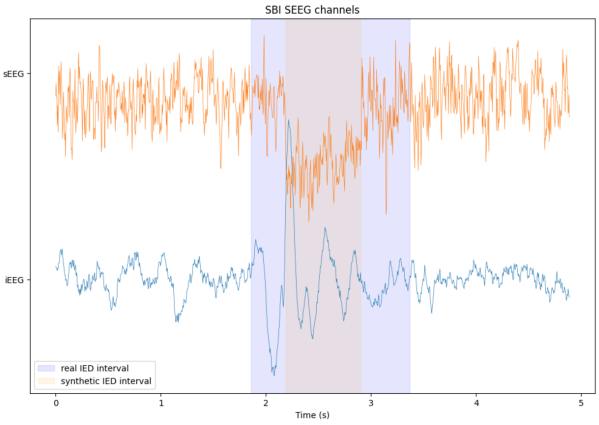

(b)

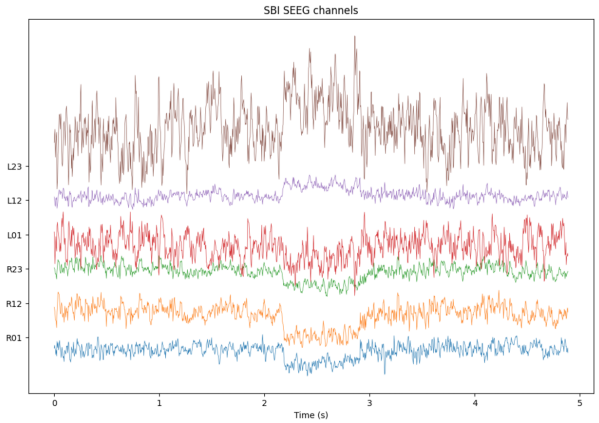

(c)

Figure 23: Results of SBI real whole time series data fitting of the 2^{nd} IED in Patient A. (a) The SBI posterior after 51,000 simulations with the maximal estimated posterior marked in orange. (b) Synthetic SBI-estimated channel and real channel (R01) plotted against time. The blue and orange marked intervals indicate the real annotated and SBI-estimated IED interval, respectively. (c) All synthetic iEEG channels from the SBI-estimated parameter set.

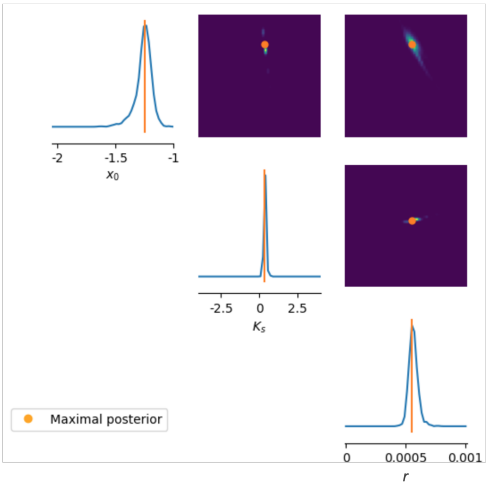

(a)

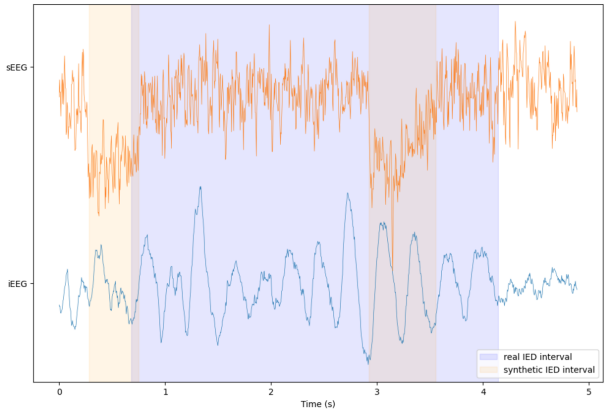

(b)

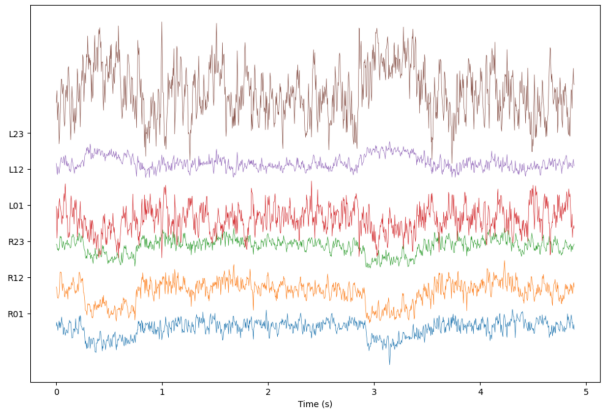

(c)

Figure 24: Results of SBI real whole time series data fitting of the 3^{rd} IED in Patient A. (a) The SBI posterior after 51,000 simulations with the maximal estimated posterior marked in orange. (b) Synthetic SBI-estimated channel and real channel (R01) plotted against time. The blue and orange marked intervals indicate the real annotated and SBI-estimated IED interval, respectively. (c) All synthetic iEEG channels from the SBI-estimated parameter set.

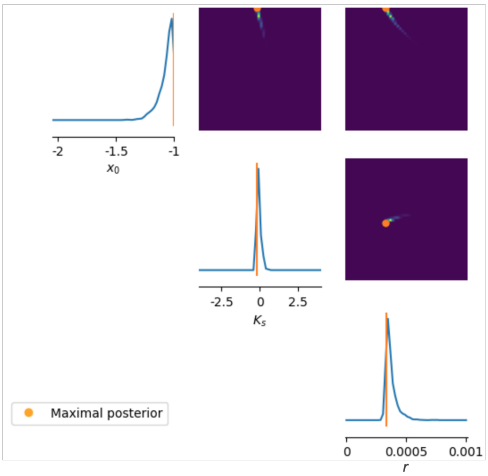

(a)

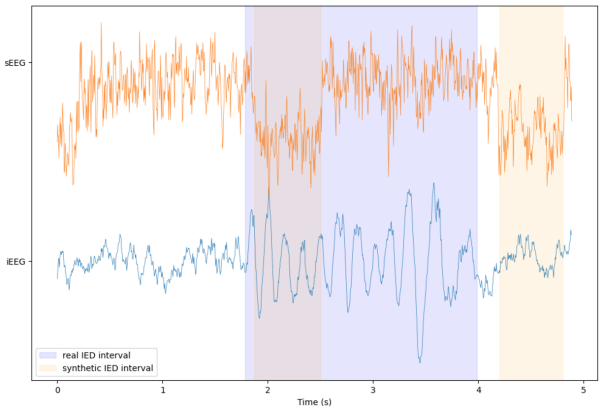

(b)

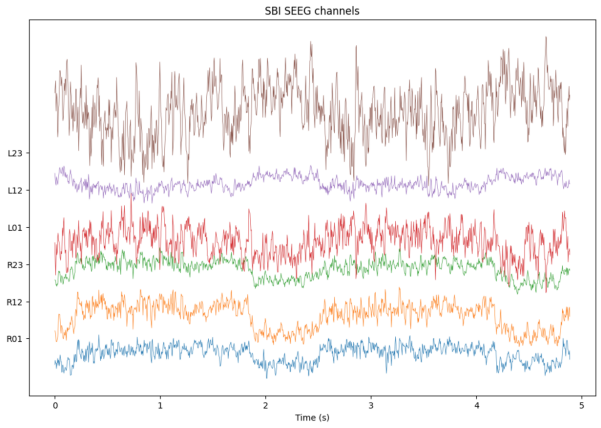

(c)

Figure 25: Results of SBI real whole time series data fitting of the 4^{th} IED in Patient A. (a) The SBI posterior after 51,000 simulations with the maximal estimated posterior marked in orange. (b) Synthetic SBI-estimated channel and real channel (R01) plotted against time. The blue and orange marked intervals indicate the real annotated and SBI estimated IED interval, respectively. (c) All synthetic iEEG channels from the SBI-estimated parameter set.

D SBI-derived and real IED duration ratio

In Figure 26, the ratio of the IED duration is given with respect to the healthy duration of the simulated interval. This is visualised against the real IED duration towards which the simulated IED duration was converged from the SBI neural network. Figure 26a and 26b illustrate this for the neural networks that were trained based on 5-second and 15-second simulations, respectively. An IED/healthy duration ratio of zero indicates no IED had been detected for the corresponding simulation, based on the maximal posterior that was found from the sampled distribution, given the real IED duration as observed data. This can be seen in both figures at the outer ranges of the simulation time, with similar minimal and maximal ratios.

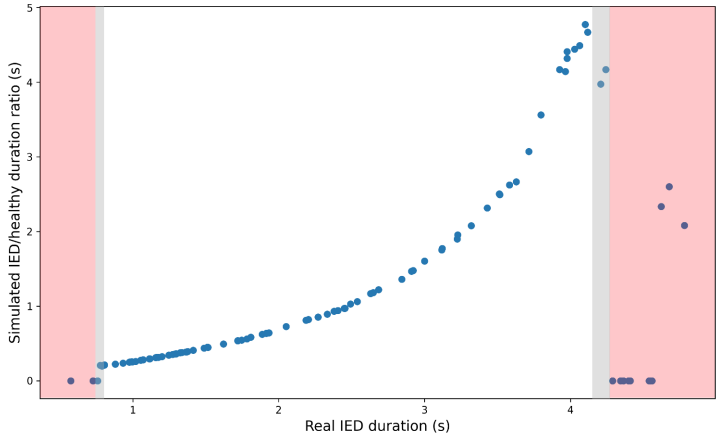

(a)

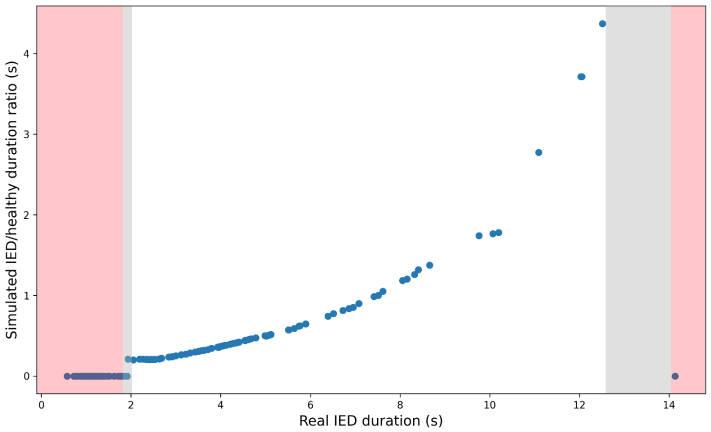

(b)

Figure 26: Visualisation of the IED-healthy duration ratios. On the x-axis, the real IED duration is given which is used as observed data for sampling the SBI posterior distribution. The maximal posterior from here is used to simulate and detect the features from which the ratio values were found on the y-axis. For (a) and (b), the ratio values are plotted as found from the 5-second-based and 15-second-based trained neural network, respectively. The figures show a resemblance in minimal and maximal detected ratio values. A ratio of zero indicates no detected IED in the simulation.